

This manuscript is a preprint and has been submitted for publication in Basin Research. Please note that the manuscript has not yet undergone peer-review and is yet to be accepted for publication. Subsequent versions of this manuscript may have slightly different content. If accepted, the final version of this manuscript will be available via the 'Peer-reviewed Publication DOI' link on the right-hand side of this webpage. Please feel free to contact the authors with any comments, we welcome feedback.

Halokinetic modulation of sedimentary thickness and architecture: a numerical modelling approach

Zoë A. Cumberpatch¹, Emma Finch¹, Ian A. Kane¹, Leonardo M. Pichel², Christopher. A-L. Jackson¹, Ben A. Kilhams³, David M. Hodgson⁴, Mads Huuse¹

¹*Department of Earth, Atmospheric and Environmental Sciences, University of Manchester, UK*

²*Department of Earth Science, Bergen University, Bergen, Norway*

³*Shell Upstream International, York Road, London, UK*

⁴*The Stratigraphy Group, School of Earth and Environment, University of Leeds, UK*

ABSTRACT

Subsurface salt flow can deform overlying strata and influence contemporaneous sedimentary processes. Studying salt-sediment interactions is challenging in the subsurface due to poor imaging adjacent to salt, and in the field due to the dissolution of halite. Discrete Element Modelling provides an efficient and inexpensive tool to model stratigraphy and deformation around salt structures, which is advantageous over other modelling techniques as it realistically recreates brittle processes such as faulting. Six 2D experiments were run representing 4.6 Myr (46,000 timesteps) to determine the effect of salt growth on syn-kinematic stratigraphy. Halokinetic deformation of stratigraphic architecture was assessed by varying sediment input rates (slow, intermediate, and fast), and increasing and decreasing them through time. Results show the realistic formation and evolution of salt-related faults which define a zone of halokinetic influence, ~3 times the width of the initial diapir. Outside of this, pre- and syn-kinematic stratigraphy are undeformed. Within this zone, syn-kinematic strata are initially isolated into primary salt withdrawal basins, onlapping and thinning towards the salt-cored high. In most models, syn-kinematic strata eventually thin across and cover the diapir roof. Thinning rates are up to six times greater within 350 metres of the diapir, compared to further afield, and typically decrease upwards (with time) and laterally (with distance) from the diapir. Outputs are compared to a subsurface example from the Pierce field, UK North Sea, which highlights the importance of considering local fluctuations in diapir rise rate. These can create stratigraphic architectures that may erroneously be interpreted to represent ‘apparent’ increases/decreases in sedimentation rate. Exposed examples, such as the Bakio diapir, northern Spain, can be used to make inferences of the expected depositional facies, below model resolution. Our models aid prediction of sedimentary unit thickness and thinning rates, and can be used to test interpretations arising from incomplete or low-resolution subsurface and outcrop data when building geological models for subsurface energy.

INTRODUCTION

Deformation by salt-tectonics influences over 120 sedimentary basins globally (e.g. Hudec and Jackson 2007; Figure 1). These basins include some of the world’s largest subsurface energy-producing provinces, such as the Gulf of Mexico (e.g. Booth et al. 2003; Hudec et al. 2013), the North Sea (e.g., Mannie et al. 2014; 2016; Charles and Ryzhikov 2015; Stricker et al. 2018; Figure 1A), offshore Angola (e.g. Oluboyo et al. 2014; Doughty-Jones et al. 2017; Howlett et al. 2020), offshore Brazil (e.g. Rodriguez et al. 2018; 2020; Pichel et al. 2019), and the Precaspian Basin (e.g. Duffy et al. 2017; Pichel and Jackson 2020). There is therefore a need to better understand the interactions of sedimentary processes and routing with topographic relief associated with salt tectonics to provide insight into sediment routing patterns around topography (e.g. Ribes et al. 2015; Cumberpatch et al. 2021a; Giles and Lawton 2002; Rowan et al. 2003; Pichel and Jackson, 2020). As a consequence, this can improve predictions of reservoir distribution and trap geometry and style for carbon storage (e.g. Maia da Costa et al. 2018; Roelofse et al. 2019), geothermal energy (e.g. Harms 2015; Daniilidis and Herber 2017; Andrews et al. 2020), and hydrocarbons (Figure 1; e.g. Hodgson et al. 1992; Jackson and Hudec 2017; Pichel and Jackson, 2020).

53
54 Constraining the dynamic evolution of the sediment-salt interface through time and space remains
55 challenging. Despite advances in the quantity and quality of 3D seismic reflection data, the salt-sediment
56 interface remains difficult to image due to poor velocity control, steep to overturned bedding and near-
57 diapir deformation (Figure 1; Jones and Davison 2014). Resolution issues caused by variable lithological
58 distributions, both within the salt and its overburden, further complicate seismic reflection-based,
59 subsurface analysis (Davison et al. 2000; Jones and Davison 2014). This leads to uncertainty in prediction
60 of facies and thicknesses via seismic methods (Figure 1; e.g. Berton and Vesely 2016; Hossain 2019).
61 Therefore, halokinetically influenced depositional systems (or portions of such systems) benefit from
62 calibration with outcrop analogues (e.g. Lerche and Petersen 1995; Jackson and Hudec 2017). Exposed
63 examples are often limited in the rock record, largely due to dissolution of halite forming the core of the
64 salt bodies (Jackson and Hudec 2017). Rare exposures provide sub-seismic scale facies information for
65 shallow- (e.g. Giles and Lawton, 2002; Giles and Rowan 2012), deep- (e.g. Poprawski et al. 2014; 2016;
66 Cumberpatch et al. 2021a) and non-marine stratigraphy (e.g. Banham and Mountney 2013a; b; 2014; Ribes et
67 al. 2015; 2017). Detailed depositional facies models can be developed from subsurface (e.g. Madof et al.
68 2009; Rodriguez et al. 2020) and outcrop datasets (e.g. Banham and Mountney 2013a; b; 2014; Cumberpatch
69 et al. 2021a) providing a useful framework that can be applied to salt-influenced basins globally. Many field
70 examples are small in size compared to subsurface basins and therefore provide only small-scale details of,
71 for example, sedimentary structures and stratal stacking patterns, rather than the larger, basin-scale
72 tectonostratigraphic context of salt-sediment interactions provided by integrated subsurface datasets. While
73 useful, each subsurface or field example represents a unique record of the ratio of salt rise and sedimentation
74 rate. Also, subsurface and field examples provide only one snapshot in time (Figure 1). Physical models
75 have an advantage in recreating the evolution of specific subsurface analogues (Dooley et al. 2013; 2015;
76 2020; Dooley and Hudec, 2017; Ferrer et al. 2017; Roma et al. 2018) and studying sedimentary gravity-
77 currents flow distribution and evolution adjacent to salt topography (Gauillier and Vendeville, 2005; Sellier
78 and Vendeville, 2010; Soutter et al. 2021).

79
80 A number of remaining questions can be addressed by taking a numerical modelling approach, that allows
81 us to modify and isolate the key controls on salt-sediment interactions. These include: 1) How does salt
82 topography influence depositional systems, and thus depositional facies, and how does this vary laterally
83 and temporally? 2) How do unconformities, onlap contacts, and faults and fractures vary in salt-influenced
84 settings? 3) How does sedimentation rate influence the width of the roof and basin salt-related deformation
85 zones? and 4) How do stratigraphic thinning rates associated with salt growth vary with sedimentation rate
86 and distance from the salt structure?

87
88 Most recent advances in numerical models use finite element models (FEM), which are based on continuum
89 methods. Such studies have focused on the physical conditions required for the initiation and development
90 of diapirism (Poliakov et al. 1993; Gemmer et al., 2004; 2005; Chemia et al. 2008; Fuchs et al. 2011;
91 Fernandez and Kaus 2015; Nikolinakou et al. 2017; Hamilton-Wright et al. 2019; Peel et al. 2020), the
92 stratigraphic architecture of subsiding minibasins (Sylvester et al. 2015; Wang et al. 2017; Fernandez et al.
93 2020), reconstructing evolutionary history of salt-affected stratigraphy (Ismail-Zadeh et al. 2001; 2004;
94 Pichel et al. 2017; 2019), and salt-related stress (and strain) analysis (Luo et al. 2012; 2017; Nikolinakou et
95 al. 2012; 2014a; b; 2018; Heidari et al. 2017). FEM often treats the overburden as a continuous frictional-
96 plastic or viscous-plastic material, which prevents the development of realistic brittle deformation (e.g.
97 fracturing and faulting) in overburden stratigraphy (Figure 1). Most FEM packages currently have limited
98 capacity to generate faults during simulations, and therefore either have no faults or faults that are pre-
99 defined at the start of the model simulation (e.g. Heidari et al. 2016; Nikolinakou et al. 2014; 2018). FEM
100 is advantageous for studying ductile deformation and salt flow dynamics (Albertz and Ings 2012).

101
102 Discrete Element Models (DEM), which essentially treat the contact between each element as a slip surface,
103 are able to replicate spontaneous, realistic, localised fault nucleation and growth (Pichel et al. 2017; 2019;
104 Cumberpatch et al. 2021b) and are therefore appropriate for studying the interactions between salt-related
105 topography, sedimentation, and stratigraphic evolution. DEM provides a quick, efficient and inexpensive
106 method to investigate system evolution through time (Allen and Tildesley 1987; Donzé et al. 1994; Finch
107 et al. 2003; 2004). It is therefore possible to test a number of scenarios and collect structural growth and
108 syn-kinematic sediment thinning rate data during deformation. This helps to improve recognition of the

109 processes involved with salt-sediment interactions. DEM studies have recently been adapted to salt
110 tectonics so that elements representing salt behave as viscous-plastic materials (Pichel et al. 2017; 2019).

111
112 Here, we use a DEM approach to understand how sedimentation rate effects stratal geometries in salt
113 basins experiencing diapirism (Figure 1). First, we generate a baseline model with no sediment fill, to
114 determine the effect of salt growth on pre-kinematic, diapir-capping stratigraphy. We define ‘pre-kinematic
115 layers’ as layers deposited prior to our simulation, they are discordant to the diapir and thus represent the
116 early diapiric syn-kinematic strata related to the phase of diapirism that is assumed to have emplaced the
117 diapir into our model (Jackson and Hudec 2017). We then vary sedimentation rate and patterns to study
118 how these control the stratigraphic record of halokinesis. The aims of this study are to: 1) investigate
119 variable syn-kinematic sedimentation rates adjacent to a dynamic salt diapir using a DEM; 2) quantify near-
120 diapir thinning rates and how this is controlled by varying sedimentation rates and patterns; and 3) compare
121 the results to subsurface and field analogues to test the validity of our approach and our model predictions.

122 DATA AND METHODS

123
124 The Discrete Element Model (DEM) applied here is a discontinuous numerical method, which derives
125 from the Particle Dynamics Method and Lattice Solid Model (Mora and Place 1993; 1994). DEMs have
126 been successfully used in physics and chemistry to study liquid and gas behaviours (Allen and Tildesley
127 1987; Hardy and Finch 2006). In geoscience, DEMs have been applied in two- and three-dimensions
128 (Longshaw et al. 2009) to forecast geological hazards, often associated with mining (Cil and Alshibli, 2012;
129 Thoeni et al. 2014; Lu et al. 2014; Zhao et al. 2016; Benseghier et al. 2020), to investigate deformation
130 caused by faulting and folding (Donzé et al. 1994; Finch 1998; Finch et al. 2003; 2004; Imber et al. 2004;
131 Hardy and Finch 2005; 2006; Schöpfer et al. 2006; Bellheine et al. 2009; Longshaw et al. 2012; Abe and
132 Urai 2012; Katz et al. 2014), and to study regional-scale salt tectonics (Pichel et al. 2017; 2019).

133
134 DEMs offer advantages over other numerical methods in that scale is not a restriction, complex re-meshing
135 is not required, and results are easily reproducible. DEMs are fundamentally discontinuous, and therefore
136 each element simulates the specific physical properties of a given rock. These conditions make it a fit-for-
137 purpose method to quantitatively study syn-kinematic deformation. DEMs do have limitations, including
138 the need for careful calibration of element parameters (Abe et al. 2011; Botter et al. 2014), and the limited
139 number of elements and the duration of simulations (Zhu et al. 2008).

140
141 DEM treats objects as assemblages of circular elements, connected by breakable elastic bonds through a
142 ‘repulsive-attractive’ force. Elements remain bonded until their breaking separation (defined as the relative
143 strength of the assemblage) is exceeded (Donzé et al. 1994; Finch et al. 2004). Once these bonds break,
144 previously connected elements experience no further ‘attractive’ force, if these elements return to contact
145 with each other a ‘repulsive’ force acts between them, preventing the healing of bonds (Finch et al. 2003;
146 2004; Hardy and Finch 2006). Motion of elements is frictionless and cohesionless with elasto-plastic
147 behaviour (Finch et al. 2003; Hardy and Finch 2007). Forces are resolved in the x and y directions and
148 elements are subject to gravity (F_g) (Finch et al. 2003). The equations that define the inter-relationship of
149 all forces acting on the DEM are:

$$150$$
$$151 F_x = F_{i,n} - V\dot{X}$$
$$152 F_y = F_{i,n} - V\dot{Y} + F_g$$

153

154 Where $F_{i,n}$ corresponds to the total elastic force acting on an element, V represents the viscosity and \dot{X} and
155 \dot{Y} correspond to the velocity of the element in the x- and y- directions. A viscous term is added to counteract
156 the elastic behaviour within a closed system, making it ideal for studying quasi-steady state tectonic
157 processes (Finch et al. 2004; Pichel et al. 2017; 2019). For a comprehensive description of the equations
158 governing DEM, see Mora and Place (1994), Finch et al. (2003; 2004), and Hardy and Finch (2005, 2006).

159
160 Pichel et al. (2017, 2019) recently used a DEM to model salt-tectonics for the first time, studying regional-
161 scale compressional salt tectonics (Pichel et al. 2017), and the effect of base salt relief on salt flow and
162 overburden deformation styles (Pichel et al, 2019). Cumberpatch et al. (2021b) adapted these models to

163 focus on the modulation of stratigraphy by salt diapir growth. In these models, the elements representing
164 salt were adjusted so they behave as a viscous-plastic material in order to represent rock-salt (Pichel et al.
165 2017; 2019). This requires inter-element interactions to be adjusted so they behave macroscopically as
166 viscous-plastic materials and deform microscopically by dislocation creep, which is expected for dry rock
167 salt (Spiers et al. 1990; Pichel et al. 2017; 2019). This does not completely reproduce salt, which typically
168 deforms on a spectrum of mechanisms including diffusion and dislocation creep (Spiers et al. 1990; Jackson
169 and Hudec 2017; Pichel et al. 2017), and usually contains traces of brines (Warren 1999; 2006), but is
170 considered a satisfactory assumption for studying salt tectonics. Pichel et al. (2017) tested breaking
171 separations (BS) using biaxial compression tests. Values representing tenths of a model unit (e.g. 0.05)
172 develop defined fault segments, and produced responses typical of brittle materials; these values are
173 therefore used to represent overburden sediment in this study. Values representing hundredths of a unit
174 (e.g. 0.001), however, show a minor elastic component (e.g. $F_{i,\alpha} \approx 0$), representing ductile viscous-plastic
175 materials that accumulate strain without significant stress variations. Consequently, a breaking separation
176 of 0.001 for salt elements is used in this study (see also Pichel et al., 2017), and other physical (Spiers et al.
177 1990) and numerical (Li and Urai 2016) experiments of salt deformation. By using this value we ensure salt
178 element motion is entirely controlled by the viscosity and gravity of the system (viscous-plastic behaviour).
179 The scaled viscosity of the salt is 1.1×10^9 Pa s, which is lower than its real-world viscosity (10^{17} - 10^{18} Pa s);
180 Hudec and Jackson 2007; Jackson and Hudec 2017), but works as a reasonable approximation when
181 compared with physical models (e.g. Vendeville et al. 1995; Dooley et al. 2009; 2012).

182
183 The modelled media in this study consists of a simulated 4.5 km by 1.5 km box, to ensure that the outer
184 boundaries do not influence the structural evolution of the model centre. The media consist of an
185 undeformable base and $\sim 44,500$ elements with varying radii (0.175-0.35 units, representing 5.25-9.75
186 metres); these are randomly distributed to reduce failure in preferential orientations within the matrix. A
187 150 m-thick salt layer is overlain by nine coloured 150 m thick pre-kinematic overburden layers. A salt
188 density of 2.2 g cm^{-3} is used, to mimic a slightly impure halite composition, comparable to many global salt
189 basins (e.g., Warren 1996; 2006; Hudec and Jackson 2007; Jackson and Hudec 2017; Grant et al. 2019) and
190 previous models (Pichel et al. 2017; 2019; Cumberpatch et al. 2021b).

191
192 We do not investigate the initial stages of diapir evolution, which have been well-studied elsewhere
193 (Trusheim 1960; Vendeville and Jackson 1992; Costa and Vendeville 2002; Hudec and Jackson 2007), and
194 instead focus on late stage diapir growth. Therefore, we simplify a complicated three-dimensional process
195 into a two-dimensional model, where we assume a linear salt wall or radially symmetric diapir was emplaced
196 by an earlier phase of diapirism; such an assumption is used in other numerical (Pichel et al. 2017; 2019)
197 and physical models (Davison et al. 1993; Dooley et al. 2009; 2012). This allows us to focus on the coupled
198 deformation-sedimentation characterising the late stage of diapir growth, when a tall pre-existing diapir may
199 be rejuvenated by compression (not modelled here) or rise due to buoyancy (active diapirism). During the
200 experiment the diapir is assumed to grow by halokinetic active rise, driven by the pressure of the overburden
201 on the salt source layer and to a lesser extent by the density difference between the salt and the overlying
202 stratigraphy (Jackson and Hudec 2017). Such growth can happen in the absence of regional tectonics,
203 although mild far-field compression or extension, which can enhance deformation rates, are likely in most
204 natural settings (Jackson and Hudec 2017). Active rise is retarded by roof thickness and strength, and salt
205 viscosity. Therefore, diapir height must be >66 - 75% of the surrounding overburden thickness for
206 substantial halokinesis to occur and the roof thickness must be <750 m (Schultz-Ela et al. 1993). In adhering
207 to this rule, we invoke an individual sinusoid, 750 m (base width) wide, 1050 m (70% of the 1500 m
208 overburden) tall diapir and thus a 450 m roof (Figure 2). The diapir geometries used in our models are
209 comparable to those observed in natural examples (Davison et al. 2000; Jackson and Hudec 2017).
210 Overburden breaking separation (relative strength; BS) increases with depth linearly from 0.023 – 0.027, in
211 agreement with increasing rock strength with depth. An overburden density of 2.4 - 2.6 g cm^{-3} is used in
212 agreement with natural and modelled examples, and increases with depth (e.g., Dooley et al. 2009; 2012;
213 Fuchs et al. 2011).

214
215 In nature, diapir growth periods are hugely variable in duration, ranging from 100,000s of years to 100s of
216 millions of years (Jackson and Hudec, 2017). Our focus on late-stage of diapir growth and using seismic
217 stratigraphic observations from natural examples (Oluboyo et 2014; Grimstad 2016), and run times of
218 previous numerical models (Pichel et al. 2017; 2019), supports our experimental run times of 46,000

219 timesteps with a timestep equivalent to 100 years (4.6 Myr in total). We impose an upwards motion of 0.023
220 mm/year, based on North Sea diapirs (Davison et al. 2000) to all elements representative of salt to mimic
221 diapir growth rate (Figure 2); this aims to replicate the volumetric salt supply rate (Q) described by Peel et
222 al. (2020). The diapir grows for 2.2 Myr (22000 timesteps) to allow the model to equilibrate creating seabed
223 or surface topography, prior to the addition of sediment (Figure 3).
224

225 Sediment is added from 2.2 Myr with a constant density of 2.3 g cm⁻³, in agreement with natural examples
226 of near seabed sediment (Tenzer and Gladkikh 2014; Rider and Kennedy 2018) and a breaking separation
227 of 0.023. Sediment is added in three 0.8 Myr (8000 time steps) stages (S1-S3, Table 1). Sedimentation rates
228 in nature are extremely variable (Sadler 1981). Here, the sedimentation rate was varied between 0.15-0.45
229 mm/year to match Cenozoic rates measured in the North Sea (de Haas et al. 1996) and the North Atlantic
230 (Whitman and Davies 1979).
231

232 We present results from six experiments: a baseline zero sedimentation model, and five models with variable
233 sedimentation rates and patterns (slow, intermediate and fast constant sedimentation, increasing and
234 decreasing). Increasing and decreasing sedimentation rates are used to replicate the local advance and retreat
235 of depositional sedimentary systems. Model set-up and parameters have been rigorously tested (Finch et al.
236 2003; 2004; Pichel et al. 2017; 2019) and are summarised in Supplementary Table 1.
237

238 **Model limitations**

239 The complex three-dimensional processes occurring in salt basins are simplified into a two-dimensional
240 model for this study. Therefore, we assume our models represent a cross-section through a three-
241 dimensional linear salt wall or radially symmetric diapir; this is likely to be an oversimplification based on
242 the complex, often asymmetric, geometries of salt structures (Hudec and Jackson 2007). Modelling in two-
243 dimensions also assumes that all processes (such as salt withdrawal and stratigraphic bed rotation) are equal
244 in all directions, which is an oversimplification (e.g. Ismail-Zadeh et al. 2004; Dutta et al. 2016; Jackson and
245 Hudec 2017; Mattson et al. 2020; Pichel and Jackson, 2020). However, this is a suitable assumption in
246 simple models that focus primarily on the role of sedimentation rate variability on the halokinetic
247 depositional record. In order to prevent circular reasoning, our model inputs do not attempt to recreate a
248 specific real world diapir, but rather a simplified universally applicable structure. The absence of more
249 complicated salt geometries (e.g. salt overhangs or welds) prevent direct comparison of the models to
250 specific settings with complicated three-dimensional salt structures (e.g. the Gulf of Mexico). However, our
251 approach allows us to generate more general, possibly transferrable insights that are applicable to global
252 salt basins. Finally, sedimentation rates are extremely variable and non-linear (Sadler 1981); thus when
253 comparing to certain analogues, 'slow' and 'fast' sedimentation (stated in Table 1) should be taken as relative
254 rates rather than absolute values. Sediments can be deposited above the diapir relief suggesting that our
255 models are most applicable to subaqueous settings, and are assumed to aggrade evenly, preventing direct
256 comparison to deltaic systems (clinoforms).

257 **RESULTS**

258
259 The model with intermediate sedimentation rate (M3) is first presented (Figure 3) to examine the
260 relationship between the rates of salt diapir rise sedimentation. Subsequent sections describe and compare
261 diapir growth, deformation and stratigraphic architectures across all models (Figure 4-8; Tables 2, 3).
262

263 **Summary of temporal relationship between halokinesis and sedimentation**

264
265 The initially horizontal basal salt layer thins adjacent to the diapir, and the diapir geometry changes from
266 initially triangular/sinusoidal to vertically elongated during evolution (Compare H with A in Figure 3); this
267 is consistent across all 6 models (Figure 3-6). Up to 45% thinning of the salt layer, ~450 m either side of
268 the diapir base, occurs in all final model outputs (Figure 3H). The growth of the diapir is accompanied by
269 withdrawal effects in the adjacent stratigraphy, which is indicated by thinning of the source layer and
270 faulting in the basal layers (layers 1-3, Figure 3; M3 on Figure 5B). Salt withdrawal and evidence for upwards
271 salt growth are shown by the basal part of the diapir narrowing between T=0 and T=2.2 Myr (0 to 22,000
272 time steps). Sediment is first introduced to all models after 2.2 Myr (22,000 timesteps; Figure 3B). Up to
273 this time, the diapir has risen such that 'pre-kinematic' layers 4 and 5 are folded during its rise and thin

274 dramatically towards the salt due to structural attenuation, accommodated by layer-parallel slip. Pre-
275 kinematic layers, originally overlying the diapir (layers 6-9, Figure 3), are passively folded as the diapir rises.
276 This results in ‘post-depositional’ layer thickening on the flanks and thinning over the crest (Figure 3B).
277 Above the diapir, a topographic high is generated with associated faulting in layers 6-9 observed in $T=2.2$
278 Myr (Figure 3B). The topographic high influences subsequent sedimentation (layers A-L) and is the focus
279 of our study of stratigraphic modulation (Figure 3C-H).

280

281 Sediment is added in Stage 1 (S1, $T= 2.2$ Myr, 22,000 time steps; Figure 3C), filling two salt withdrawal
282 basins either side of the diapir. For simplicity, following the methodology of Pichel et al. (2017), the first
283 syn-kinematic layer, Layer A, fills to a flat base level in all models, and subsequent layers are input by
284 assigned sedimentation rate (in the case of M3, 0.3mm/yr). Later in S1 ($T= 3$ Myr, 30,000 time steps, Figure
285 3), the rate of deposition outpaces diapir rise. Layers extend across the salt rather than onlapping it (Figure
286 3C, D). Throughout diapir rise, pre-kinematic stratigraphy is rotated away from the diapir crest, thickening
287 in the adjacent depocentres, due to structural layer-parallel slip. The diapir stem narrows throughout
288 evolution (compare H and A, Figure 3). The thinning of pre-kinematic layers above the rising diapir
289 continues into S2, where pre-kinematic layer 5 approaches vertical at the salt-sediment interface (Figure 3E,
290 F). Upward movement of the diapir is associated with, and driven by, salt withdrawal underneath the basins,
291 and increased displacement of faults at the base of the model (layers 1-4; Figure 3; M3 in Figure 5B).

292

293 In the final stage (S3), the pre- and syn-kinematic stratigraphy thin above the diapir crest, and are further
294 rotated and thicken into the salt withdrawal basins (Figure 3G, H). Faulting is present above the diapir tip
295 propagating through the pre-kinematic and into the syn-kinematic sediment (M3 in Figure 5B). Throughout
296 diapir evolution, the dip of the pre-kinematic layers increases towards the structure, and thus the
297 overburden anticline steepens and narrows as sedimentation progresses (compare H with B in Figure 3).
298 The deformation in the pre-kinematic overburden, described here, is similar across all models (M1-6).

299

300 The fault furthest from the diapir is taken as the edge of the halokinetically-influenced part of the
301 succession, which is ~ 1150 m wide on either flank (from diapir centre to fault edge), resulting in an ~ 2300
302 m zone of diapiric-influence, in all models. Outside this zone, pre- and syn-kinematic strata appear
303 undeformed. Salt mobility has a limited influence on sediments at the extremities of M3, which is consistent
304 across all models, so in subsequent figures only the central 3000 m is shown (grey box, $T = 4.6$ Myr, Figure
305 3).

306

307 To permit comparison of stratigraphic variability across all models, subsequent figures (Figure 4-6) present
308 all models (M1-M6) at the end of the experiment ($T=4.6$ Myr). In the following section, we describe and
309 compare diapir growth and roof folding, and stratigraphic architecture. In each case, we first present and
310 discuss M1, the case where there is no sediment input for comparison with models in which sedimentation
311 rate is constant (M2-M4), increasing (M5) and decreasing (M6).

312

313 **Diapir growth and roof folding**

314

315 *Diapir Rise with No Sedimentation (M1)*

316

317 In M1, the diapir crest rises a total of 425 m, and the final width of the pre-kinematic folded roof, taken
318 from the greatest change in dip in pre-kinematic layer 9 is 961 m (Figure 4; Supplementary Figure 1). These
319 values represent the base-case to compare the effect of different sedimentation rates on the final geometry
320 of the salt structure and the pre- and syn-kinematic stratigraphic architectures (Table 2, 3; Figure 5, 6).

321

322 *Constant sedimentation rates (M2-M4)*

323

324 Under slow (M2), intermediate (M3) and fast (M4) constant sedimentation rates the diapir rises by 393 m,
325 363 m and 297 m, respectively (Figure 5). Diapir growth compared to M1 is reduced by 8%, 15% and 30%
326 for the different aggradation cases, respectively (Table 2). The width of the pre-kinematic folded roof
327 decreases from 961 m in M1 to 770 m (M2), 760 m (M3) and 734 m (M4), which accounts for 20-24%
328 reduction relative to M1. Where syn-kinematic stratigraphy is present across the model (i.e. not in M2), the
329 syn-kinematic folded roof is measured from the point within layer F where there is the greatest change in

330 dip (Supplementary Figure 1). Layer F is chosen as it is the first layer that is laterally extensive across all
331 models (M3-6). The syn-kinematic folded roof is 839 m and 890 m wide in M3 and M4, respectively. The
332 syn-kinematic roofs are therefore 110% and 120% greater than the width of the pre-kinematic folded roof
333 in the same models (Supplementary Figure 1).

334

335 *Variable Sedimentation Rates: Increasing (M5) and Decreasing (M6) sedimentation rates*

336

337 In M5, under increasing sedimentation rate, the diapir rises by 368 m, a reduction of 14% compared to M1.
338 Under decreasing sedimentation rate conditions (M6) the diapir rises by 346 m, a 19% reduction when
339 compared to the base case M1 (Table 2; Figure 6, 7). The pre-kinematic folded roof width is reduced to
340 ~750 m in both models, a decrease of 22% compared to M1 (Table 2; Figure 7). The syn-kinematic folded
341 roof is 723 m and 872 m in M5 and M6, respectively, representing a 4% reduction and 16% increase
342 compared to the pre-kinematic folded roof in the same model.

343

344 **Effect of sedimentation rate on stratigraphic architecture**

345

346 Here, we discuss the lateral extent, thinning rates, and termination styles of stratigraphy onto the
347 topographic high for M2-6. In all models, layer A fills to a fixed base level, and therefore does not represent
348 the sedimentation rate of S1, so the first layer described is layer B. Stratigraphic architecture and thinning
349 rates (Table 3) are discussed with reference to three points that remain fixed throughout all models: the
350 crest, flank and undeformed zone (see uninterpreted M2 in Figure 5).

351

352 *Constant sedimentation rates (M2-M4)*

353

354 Syn-kinematic layers (B-L) are not laterally extensive in M2; this model is defined by slow sedimentation
355 rates. In this case, deposition is restricted to primary salt withdrawal basins, with no sedimentation occurring
356 over the crest of the pre-kinematic anticline. All layers terminate adjacent to the diapir, with the uppermost
357 layers (I –L) overlapping the remnant topography created by the layers below (Figure 5). The entire
358 stratigraphic package thins by 34%, at a rate of 0.029%/m from the undeformed zone to salt flank, before
359 pinching-out towards the crest.

360

361 In M3, the model defined by intermediate sedimentation rates, the earliest syn-kinematic strata (Layers B
362 and C) are preserved only in the withdrawal basin, offset some distance from the diapir (Table 3). However,
363 in contrast to M2, layers D-L are laterally extensive across the model, extending across the diapir crest
364 (Table 3). The overall stratigraphic thinning for intermediate aggradation is 55% from undeformed to crest,
365 at a rate of 0.037%/m, with 35% of this occurring between the undeformed and flank, accounting for 19%
366 thinning at a rate of 0.017%/m. Thinning rates of 0.1%/m, totalling 35% stratigraphic thinning, are
367 observed from flank to crest. The thinning rate between the salt flank and the crest is ~ 6 times greater
368 than that between the undeformed section and the flank (Table 3).

369

370 In the fast sedimentation model, M4, all layers are extensive across the model except for layer B (Figure 5;
371 Table 3). The overall stratigraphic thinning for fast aggradation is 33% from undeformed to crest at a rate
372 of 0.022%/m. Thirty-five percent of this total thinning is between the undeformed section and the salt
373 flank, accounting for 12% stratigraphic thinning at a rate of 0.01%/m, and the other 65% occurs between
374 the salt flank and the crest with a thinning rate of 0.06% accounting for 21% stratigraphic thinning. The
375 thinning rate between the salt flank and the crest is ~6 times greater than that between the undeformed
376 section and the flank (Table 3).

377

378 *Variable Sedimentation Rates: Increasing (M5) and Decreasing (M6) sedimentation rates*

379

380 In M5 (increasing sedimentation rate), layers B-D represent slow sedimentation; these layers are restricted
381 to the salt withdrawal basin either side of the structure and thin-towards the salt influenced topography
382 before pinching out. Layers E-H were deposited under intermediate sedimentation rates. Layer E does not
383 extend across the model and thins towards topography between the undeformed section and the salt flank,
384 before pinching out towards the crest. Layers F-H are extensive across the model. Layers I-L were deposited
385 under the fast sedimentation rate, and are laterally extensive across the entire model (Figure 6; Table 3).

386 Overall thinning in the increasing sedimentation model accounts for 58% total stratigraphic thinning at an
387 average rate of 0.039%/m; 67% of this thinning takes place between the salt flank and the crest, accounting
388 for 39% stratigraphic thinning at a rate of 0.11 %/m. The remaining 33% of thinning occurs between the
389 undeformed section and the salt flank, at a rate of 0.017%/m accounting for 19% stratigraphic thinning.
390 The thinning rate between the salt flank and the crest is 6.6 times greater than that between the undeformed
391 section and the salt flank (Table 3).

392
393 In M6 (decreasing sedimentation rate), layers B-D represent fast sedimentation. Layer B is isolated to either
394 side of the diapir and thins between the undeformed section and the flank before terminating towards the
395 diapir (Table 3). Layers C and D are laterally extensive. Layers E-H represent intermediate sedimentation,
396 and are deposited across the entire model. Layers I-L are deposited under slow sedimentation and are
397 extensive across the whole model, but thin markedly over the crest (Figure 6; Table 3). The overall
398 stratigraphic thinning for the decreasing sedimentation rate model is 52% at a rate of 0.035%/m. Thirty-
399 five percent of this thinning takes place between the undeformed section and the diapir flank, accounting
400 for 19% stratigraphic thinning at a rate of 0.016%/m, and the remaining 65% thinning occurs between the
401 flank and the crest, at a rate of 0.097%/m, accounting for 34% stratigraphic thinning. The thinning rate
402 between the salt flank and the crest is ~6 times greater than that between the undeformed section and the
403 salt flank (Table 3).

404 **SUMMARY OF HALOKINETIC INFLUENCE**

405 **Diapir growth and roof folding**

406
407 In our model, we invoke a constant upward movement, or growth, of the salt diapir. Therefore, our models
408 show how different sedimentation rates can dampen the late-stage growth of diapirs. The greatest upward
409 movement of the diapir is observed in the model with no sedimentation (M1) (Table 2; Figure 7), because
410 in this case there is no roof to resist the upward flux of salt. M1 is taken as the base case. Upward movement
411 (growth) of the diapir is reduced with the addition of sediment (Table 2; Figure 5, 6), which in essence
412 increases the roof thickness towards the limit where diapir growth can occur (i.e. diapir height approaches
413 <66% of overburden: Schultz-Ela et al. 1993). The amount of growth reduces, compared to the base case
414 (M1), with increasing sedimentation rate (being limited to 70% in M4), showing that sedimentation rate is
415 a key control on burial of salt topography. This observation is in agreement with existing models (Giles and
416 Lawton 2002; Hudec and Jackson 2007; Fuchs et al. 2011; Jackson and Hudec 2017; Peel et al. 2020). We
417 also note that the anticline defining the *pre-kinematic* folded roof is widest in M1 and decreases with
418 increasing sedimentation rate (Table 2; Figure 7, 9). However, the anticline within the *syn-kinematic* folded
419 roof is widest in M4, appearing to increase with increasing stratigraphic thickness (i.e. sedimentation rate).
420 In models with added sedimentation (M2-M6), the pre-kinematic roof anticline is 20-24% narrower than
421 in M1 (no sedimentation). The lack of variability between different sedimentation conditions may imply
422 that sedimentation rate has only a minor control on pre-kinematic anticline width, with other controls such
423 as salt supply, salt viscosity and regional tectonics (not modelled) being more important (Koyi 1998; Fuchs
424 et al. 2011). Syn-kinematic folded roof thicknesses are more variable across the models, because they are
425 controlled by the sedimentation rate. Increasing syn-kinematic folded roof width with sedimentation rate
426 supports fold wavelengths being larger for thicker overburdens (Davison et al. 2000b; Bonini 2003; Hudec
427 and Jackson 2011; Duffy et al. 2018).

429 **Fault distribution and deformation zone extent**

430
431 Fault distribution and withdrawal basin extent are interpreted using the nearest neighbour outputs (Figure
432 4; Supplementary Figure 2). Nearest neighbour outputs highlight the amount of displacement that has
433 occurred during 4.6 Myr, relative to an element's initial neighbours; this is used to highlight discontinuities
434 as a proxy for faults. Fault distributions are broadly similar across all models (Figures 4-6) and are
435 summarised here. Numerous predominantly extensional faults, with variable dip directions, are identified
436 in the pre-kinematic layers in all experiments. These faults have displacements of metres to 100's of metres,
437 with the greatest throws being observed between pre-kinematic layers 1-7 (Figures 4-6). Steep structures
438 appear to develop over the crest of the growing diapir, but are difficult to decipher in terms of slip style
439 (i.e. normal or reverse) due to the relatively small number of displaced neighbouring elements. These crestal
440 structures extend into the syn-kinematic strata (layers A-G) overlying the overburden anticline (M3-M6);

441 these discontinuities are largest and extend furthest into the syn-kinematic overburden under greater
442 sedimentation rates (compare M4 with M3; Figure 5). In all experiments, pre-kinematic layers 8 and 9 are
443 dominated by small-scale faults that are localised to those layers.

444

445 The edge of the salt withdrawal basin is taken as the distance of the furthest faults from the diapir; outside
446 this zone the strata are not deformed (Figure 4-6). The salt withdrawal basin, and associated deformation
447 zone, is ~2300 m wide in all models, accounting for three times the initial maximum width of the diapir
448 (Figure 4-6). The similar extent of the withdrawal basin across all experiments suggests that syn-kinematic
449 sedimentation only has a minor control on deformation of pre-kinematic layers and structural
450 configuration.

451

452 **Stratigraphic architecture variability with sedimentation rate**

453

454 Here, the variability in thinning rate is compared between different models with syn-kinematic
455 sedimentation. Layer A is excluded from descriptions in all models, and thus from our comparisons, as it
456 fills to a linear, instantaneous base level and therefore does not always represent the sedimentation rate of
457 S1. Therefore 11 layers (B-L) are described and compared in Table 3.

458

459 Under slow sedimentation rate (M2) all 11 layers onlap topography and are not laterally extensive. Under
460 intermediate sedimentation rate (M3) two layers onlap and nine are laterally extensive, rising to 10 laterally
461 extensive and one onlapping in the fast (M4) and decreasing (M6) sedimentation rate cases. Under
462 increasing sedimentation rate (M5), the initial four layers (including three which are deposited under slow
463 sedimentation) onlap topography and the remaining 7 are laterally extensive (Figure 5). As expected, layers
464 are more laterally extensive under higher sedimentation suggesting that the effects of halokinetic
465 modulation decrease more rapidly upwards under higher sedimentation rates (Peel et al. 2014; Sylvester et
466 al. 2015; Cumberpatch et al. 2021b). The final stratigraphic thickness is greatest under fast sedimentation
467 rate (M4, 570 m), least under slow sedimentation rate (M2, 228 m), and at a similar intermediate level for
468 intermediate (M3, 401 m), increasing (M5, 441 m) and decreasing (M6, 382 m) sedimentation rates, logically
469 showing that net sediment volume is the most important control on sediment thickness (Figure 7, 8, 9).

470

471 Overall stratigraphic thinning, from the undeformed to the flank, is greatest under slow sedimentation rate
472 (M2, 34% thinning) and least under fast sedimentation rate (M4, 12% thinning) (Table 3). This shows that
473 stratigraphic thinning rates decrease with increasing sedimentation, suggesting that diapir modulation
474 (thickness and dip variability) decreases quicker under higher sedimentation rate (Pratson and Ryan 1994;
475 Koyi 1998; Fuchs et al. 2011).

476

477 In all models, the thinning rate is ~ 6 times greater between the salt flank and the crest than it is between
478 the undeformed section and the salt flank (Table 3; Figure 9). This rate is higher (6.6 times) under increasing
479 sedimentation (M5), which suggests that salt structures have greater influence in models where
480 sedimentation rate is initially slow (e.g., S1 in M5; Giles and Lawton 2002; Fuchs et al. 2011; Giles and
481 Rowan 2012; Jackson and Hudec 2017).

482

483 Whilst the primary mechanism modulating the stratigraphic architecture is stratigraphic thinning,
484 stratigraphic thickening into basins driven by salt withdrawal at depth must not be disregarded. Localised
485 thickening into salt withdrawal basins is observed in all models. Such thickening is observed in all models,
486 accounting for 13% of the stratigraphic thickening in M5 (Cumberpatch et al. 2021b). This highlights how
487 the presence of a growing diapir can be associated with localised additional accommodation (as well as a
488 reduction of accommodation) due to the at-depth evacuation of salt from the source layer to feed the
489 growing diapir, as is evidenced by subtle thickening into the basin (Figure 5; 6). Accommodation reduction
490 over the crest of the diapir is driven by diapir growth, which is recorded by stratigraphic thinning.
491 Accommodation increases in salt withdrawal basins are accounted for by stratigraphic thickening and salt
492 migration at depth.

493

494 Through time, thickening and thinning are eventually reduced as the halokinetic modulation on stratigraphy
495 is minimised with the burial of the salt-cored topographic high and its flanking depocentres. In all
496 experiments with layers that extend across the entire model, the thinning rate and bedding orientation

497 change up-stratigraphy (Table 3, Figure 8). In M3-M5, a decrease in thinning rate up-stratigraphy is
498 observed. Bedding orientations are variable but generally decrease (flatten) upwards in M2-5. However,
499 under decreasing sedimentation (M6) an overall increase in thinning rate up-stratigraphy is observed (Figure
500 6; Table 3), in addition to a slight increase in bedding dip between layers J, K and L. This suggests that
501 initially thicker layers are less deformed, but that as diapir growth continues and sedimentation decreases,
502 thin layers are still influenced by topography associated with rising salt (Giles and Lawton 2002; Hudec and
503 Jackson 2007; Giles and Rowan 2012; Sylvester et al. 2015; Soutter et al. 2019).

504

505 Overall, halokinetic modification reduces with increasing sedimentation rate as halokinetic bathymetry is
506 buried. Typically, such alteration decreases up stratigraphy, and laterally outwards from the diapir in
507 agreement with outcrop and subsurface analogues globally (Figure 9, 10, 11; e.g. Pratson and Ryan 1994;
508 Giles and Lawton 2002; Mayall et al. 2010; Giles and Rowan 2012; Kernen et al. 2012; 2018; Banham and
509 Mountney 2013a; 2013b; 2014; Oluboyo et al. 2014; Poprawski et al. 2014; 2016; Ribes et al. 2015; Doughty-
510 Jones et al. 2017; Wu et al. 2020; Rodriguez et al. 2020; Cumberpatch et al. 2021a).

511

512 **DISCUSSION**

513

514 **Comparison to natural examples**

515

516 A key challenge for numerical models is ground-truthing against natural prototypes (Oreskes et al. 1994;
517 Burgess 2012). Here, the key findings and predictions from the DEM (Figure 9) are compared to published
518 subsurface (Figure 10,11) and field analogues (Figure 12) to understand their applicability and limitations.

519

520 *Comparison to subsurface: stratigraphy around the Pierce diapirs, Eastern Central Graben, UK North Sea*

521 Jurassic-Pleistocene syn-kinematic stratigraphy around the north and south Pierce diapirs, Eastern Central
522 Graben, UK North Sea (Figure 10) shows evidence for halokinetically driven changes in bed thickness and
523 dip (Figure 11C, 10E; Birch and Haynes 2003). Pierce's tectonostratigraphic history spans ~200 Myr and
524 is summarised as Jurassic reactive-active diapirism, followed-by Cretaceous-Cenozoic passive diapirism,
525 and contraction-driven active diapirism during Alpine compression (Scott et al. 2010). Despite a longer-
526 lived and more complex evolution, the Pierce diapirs show geometrical similarities with several of our
527 DEMs (Figure 9, 10). In the Pierce example, stratigraphy is near horizontal ~2 km away from both diapirs,
528 but is upturned adjacent to them, comparable with model results (Figure 5, 6, 9, 10). The generation of
529 brittle deformation throughout the Cenozoic stratigraphy over the crest of both north and south Pierce
530 (Figure 11; Carruthers et al. 2013) corresponds to high zones of relative displacement across the crest of
531 the diapir, in M3-M6, which extend into the syn-kinematic stratigraphy (Figure 5, 6, Supplementary Material
532 1). Similar crestal deformation has been demonstrated in physical models (e.g., Davison et al. 1993).
533 Different model outputs may be applicable to different parts of stratigraphy due to the changing ratio of
534 diapir rise rate and sedimentation rate. For example, stratigraphic architectures comparable to M2, M3 and
535 M5 are observed in different stratigraphic packages around the Pierce diapirs (Figure 11).

536

537 The unique observation from M2 (slow sedimentation) is non-extensive layers that thin towards and
538 eventually onlap and pinchout against the long-lived, salt-related topographic high (Figure 9A). M2 results
539 are analogous to the Top Cretaceous (lime green) to Mid Eocene (red) stratigraphy around the Pierce diapirs
540 (Figure 11C), which is not laterally extensive across the diapirs (Davison et al. 2000a; Birch and Haynes
541 2003; Scott et al. 2010; Carruthers et al. 2013). The Top Cretaceous – Mid Eocene package, equivalent to
542 S1-S3 in the models, thins significantly towards both diapirs, before onlapping the flanks (Figure 9A; 10A;
543 10C). The amount and rate of thinning reduce through time, from 51% at 0.044%/m in the Paleocene (Top
544 Cretaceous – Top Lista interpretations) to 21.3% at 0.019%/m between in the Eocene (Tay and Eocene
545 interpretations (Supplementary Table 2) in agreement with model observations showing thinning rates
546 reducing upwards. These values are similar to the overall thinning of the slow sedimentation model (34%,
547 at 0.029%/m; Table 3). Despite this apparent similarity in thinning rate values, regional sediment volumes
548 are high throughout the Palaeocene (10,000 km³/my; Lui and Galloway 1997). Specific lithostratigraphic
549 units such as the Forties Sandstone are associated with ~200 m of sandstone deposited in c. 1 million years
550 (Kilhams et al. 2014; Eldrett et al. 2015). Sedimentation rates for the UK Palaeocene stratigraphy are
551 uncertain, and spatially and temporarily variable around the Pierce diapirs, with rates ranging from 0.085 -

552 0.4 mm/yr (Liu and Galloway 1997; Kilhams et al. 2014; Eldrett et al. 2015). The lower values are in broad
553 agreement with our slow sedimentation input values. The upper end, however, indicates intermediate – fast
554 sedimentation rates in our models, which have probably been modified by very high diapir rise rates to
555 form an overall geometry typical of slow sedimentation rates (Carruthers et al. 2013). This is further
556 evidenced by the steep upturning of stratigraphy adjacent to the diapirs (Figure 11C; Giles and Lawton
557 2002; Hudec and Jackson 2007). In our model, we isolate and vary sedimentation rate, whilst in reality the
558 dynamic ratio of sedimentation rate and diapir rise rate control stratigraphic architecture. It is suggested
559 that during the Paleocene – Eocene sedimentation rates were high, but diapir rise rates were higher, likely
560 driven by sediment loading (Carruthers et al. 2013) creating an overall effect of a ‘low sedimentation rate’
561 akin to our M2.

562
563 In M3 (intermediate sedimentation rates), layers are initially non-extensive (S1), displaying early onlap and
564 thinning (26.4% at 0.023 %/m; Table 3; Figure 9B; 10B) similar to Eocene (orange) to Oligocene (peach)
565 stratigraphy adjacent to the north Pierce diapir (Figure 11), which thin by 16% at 0.014 %/m. Subsequent
566 modelled layers (S2) are extensive but thin towards the diapir high (60% at 0.04 %/m; Table 3), analogous
567 to the Oligocene (peach) to Mid-Miocene (light peach) across north Pierce (65% at 0.044 %/m;
568 Supplementary Table 2; Figure 11C; Carruthers et al. 2013). In our model simulations, 76% of this thinning
569 occurs between the undeformed and the flank location, similar to subsurface observations of 85% thinning
570 around north Pierce. After this initial modulation (S1, S2), subsequent M3 stratigraphy (S3) records a
571 reduction in thinning rates and halokinetic influence on stratigraphy upwards (reduction from 60% to 23%
572 total thinning: Table 3; Figure 9B; 10B). This is also observed, albeit at a less extreme rate, between the
573 Middle Miocene and Pliocene interval around the Pierce diapirs (reduction from 65% to 49% total thinning;
574 Supplementary Table 2; Figure 11). Much of the excess thinning in the Pierce example, compared to the
575 model, occurs between the undeformed and flank position (28% of thinning, compared to 6% in M3; Table
576 3, 4). This is likely due to Cenozoic compressional forces driving diapir growth and upturn of stratigraphy
577 (Birch and Haynes 2003; Scott et al. 2010; Carruthers et al. 2013), resulting in a less gradual reduction in
578 halokinetic alteration upwards with respect to M3.

579
580 Based on this comparison of the lateral extent of layers, it is possible to infer that these examples represent
581 intermediate sedimentation rates, relative to diapir rise rate. Sedimentation volumes for the Eocene to
582 Oligocene are ~4000 km³/Myr, lower than for the Top Cretaceous-Eocene. This suggests that overall diapir
583 rise rate had been slower during the Eocene to Oligocene, with respect to the Top Cretaceous-Eocene
584 time, giving a stratigraphic architecture typical of lower diapir rise rates relative to sedimentation rates
585 (Carruthers et al. 2013).

586
587 In M5 (increasing sedimentation rate), S1 and early S2 are initially isolated either side of the diapir in salt-
588 withdrawal basins and onlap salt-cored topography (Table 3). Late S2 stratigraphy is extensive across the
589 model, thinning towards the topographic high, with modulation decreasing up-stratigraphy (S3, Figure 9D).
590 When combining the Cretaceous to Eocene (M2 analogue, Figure 11) and Eocene to Mid-Miocene (M3
591 analogue) stratigraphy adjacent to the Pierce diapirs, we observe an overall increasing upwards
592 sedimentation trend, relative to diapir rise rate (Den Hartog Jager et al. 1993; Jennette et al. 2000; Birch and
593 Haynes 2003; Kilhams et al. 2014). The Cretaceous to Eocene was deposited when sedimentation rate <
594 diapir rise rate, leading to isolation of salt withdrawal basins and onlapping of the diapir flanks (S1, M5,
595 Figure 11D; Carruthers et al. 2013). The Eocene – Mid Miocene (S2 equivalents) were likely deposited
596 when sedimentation rates were higher relative to diapir rise rates, or when salt supply was equal to
597 sedimentation rate (S2, M5, Figure 11D; Carruthers et al. 2013). Subsequent layers (Mid-Miocene –
598 Pleistocene) are broadly extensive across the diapirs, similar to S3 in M5. The sedimentation volume for
599 this interval is fairly low (~2000 km³/Myr; Liu and Galloway 1997), so this observed reduction in
600 halokinetic influence upwards is likely driven by a slowing or cessation of diapir growth rather than being
601 driven purely by high sedimentation rates (Carruthers et al. 2013). Pliocene to Pleistocene stratigraphy is
602 extensive across north Pierce (S2 and S3, M5), but only the Pleistocene is present extensively across south
603 Pierce, due to differential diapir growth histories and cessations (Scott et al. 2010; Carruthers et al. 2013).
604 The upwards reduction in sedimentary thinning observed in the increasing sedimentation model (61% in
605 S2 to 22% in S3) is similar to that observed between the Eocene to Mid-Miocene (88%) and the Mid-
606 Miocene to Pleistocene (18%) in the subsurface example, highlighting the potential applicability of the
607 results from our models.

608
609 In nature, halokinetic sequence architecture is controlled by the dynamic ratio between sedimentation rate
610 and diapir rise rate (e.g. Giles and Rowan 2012; Pichel and Jackson, 2020), such that an ‘apparent’ increase
611 in sedimentation (reducing halokinetic influence upwards) could represent a slowing of diapir growth due
612 to regional tectonic quiescence or depletion of the salt source layer. Our observations and comparison to
613 DEMs with variable sedimentation rates, are consistent with diapir rise to sedimentation rate ratios derived
614 from halokinetic sequence studies (Carruthers et al. 2013). The role halokinesis plays in shaping the
615 stratigraphic architecture of the north and south Pierce diapirs is reduced from the Oligocene and Pliocene
616 respectively, due to source layer depletion, resulting in halokinetic bathymetry being gradually buried (Figure
617 11; Birch and Haynes 2003). Integration of, and comparison between DEM and subsurface data,
618 demonstrates the importance of understanding local (salt layer variations) and regional (tectonic and
619 sedimentation rate) controls when disentangling salt basin evolution.
620

621 *Comparison to outcrop: stratigraphy around the Bakio diapir, northern Spain*

622 The model simulations presented here document stratigraphic architectures and structural deformation, but
623 do not invoke a specific sedimentary environment. Different compositions (e.g., carbonate or siliciclastic)
624 and sedimentary environments (e.g., fluvial or deep-water) will respond differently to salt influence (Adams
625 and Kenter 2012). Below, we compare the observations of M5 (increasing sedimentation) to a well-exposed
626 halokinetically-influenced deep-water succession, and describe how integrating DEM results with
627 outcropping examples can help reduce uncertainty in subsurface energy reservoir prediction.
628

629 Exposed Aptian-Cenomanian strata adjacent to the Bakio Diapir, northern Spain document an increase in
630 sedimentation rate associated with an increase in erosion of the hinterland (Figure 12; García-Mondéjar
631 1996; Martín-Chivelet et al. 2002; Puelles et al. 2014). The resulting progradational pattern manifests in the
632 deep-water succession as an upward change from thin-bedded low-density turbidites, deposited in the lobe
633 fringe, to thick-bedded high-density turbidites deposited in a lobe axis (Cumberpatch et al. 2021a). Pre- (the
634 Urgonian limestone: Figure 12) and syn- kinematic depositional elements are deformed closest to the diapir,
635 and deformation intensity decreases away from the diapir, being minimal outside the halokinetically
636 influenced sequence (~700 m wide either side at Bakio); this observation is consistent with the predictions
637 of our model (Figure 6, 12). Outside the zone of halokinetic deformation, in terms of their architecture and
638 facies distributions, strata look similar to those deposited in an unconfined, salt-free setting (e.g., Prélat et
639 al. 2009: Figure 12D).
640

641 The Aptian-Albian is initially isolated either side of the diapir, with individual beds thinning and pinching
642 out towards the salt-cored topographic high (S1, Figure 12) (Cumberpatch et al. 2021a). Under increasing
643 sedimentation rates, the Albian-Cenomanian stratigraphy is laterally extensive and stratigraphy show a
644 reduction in the numbers of mass transport deposits (MTD) upwards. The stratigraphy also show a
645 reduction in halokinetic deformation and thinning rate upwards (S2), eventually healing remnant diapiric
646 topography (S3). In the syn-kinematic stratigraphy, thick-bedded sandstones deposited in channels and
647 lobes dominate topographic lows, where sedimentary flows were around salt-cored topographic relief
648 (Figure 12D; Mayall et al. 2010; Sylvester et al. 2012; Doughty-Jones et al. 2017; 2019; Rodriguez et al.
649 2020). Towards the highs, the lower-density part of the flows may run-up topography depositing thinly-
650 bedded muddier sandstones towards the pinchout (Figure 12E; Kneller and McCaffrey 1999; Soutter et al.
651 2019). Crestal deposition is limited due to elevation, until sedimentation period 3 (S3) where halokinetic
652 bathymetry is healed.
653

654 **Implications for subsurface energy**

655 Despite advances in extent and resolution of 3D seismic reflection imaging, the salt-sediment interface
656 remains difficult to image, yet determining its position and precise geometry is crucial in helping to appraise
657 stratigraphic-structural traps for hydrocarbon, carbon storage, and geothermal prospects globally (Jones
658 and Davison 2014; Warren 2016). Utilising outcrop analogues (Figure 12) can help provide sub-seismic
659 scale depositional facies information, helping reduce uncertainty in reservoir quality and distribution.
660 Numerical modelling results do not represent specific analogue conditions nor a ‘snapshot’ in time, and
661 they can therefore help to quickly identify generic depositional architectures, deformation patterns and
662 sediment thickness relationships as a function of several forcing parameters, such as variations in
663 sedimentation rates.

664
665 Using stratigraphic architectures from our DEM and sedimentological data from field examples, we can
666 improve predictions of the likely architecture of syn-kinematic stratigraphy and sedimentology around salt
667 structures, which are poorly-imaged in seismic reflection data. Understanding this requires a multi-scalar
668 and multi-technique approach. For example, models provide details about gross thickness changes and
669 geometry, whereas field analogues enable inferences about reservoir quality and net-to-gross.

670
671 *Depositional reservoir quality*

672 Regardless of the amount of sedimentation, our models show that stratigraphy thins as it approaches the
673 diapir, suggesting a reduction in the amount of total reservoir close to the structure (Figure 8; Jackson and
674 Hudec 2017). Siliciclastic depositional environments show a thinning of sandstone towards the topographic
675 high and an overall concentration of high reservoir quality units at the base of topography (Figure 12A; D),
676 such that a salt-related combined structural-stratigraphic trapping mechanism becomes unlikely (Figure 13;
677 Kane et al. 2012; Stricker et al. 2018). Muddier (lower reservoir quality) and thinner (lower net-to-gross)
678 units are expected closer to the diapir (Figures 8; 10E; 11; Banham and Mountney 2013; Cumberpatch et
679 al. 2021a). These units are more likely to be over-pressured due to upward rotation, creating a large pressure
680 head, with the topseal rocks unable to hold back a significant hydrocarbon column (Figure 13; Nikolinakou
681 et al. 2014a; b; 2018; Heidari et al. 2017; 2019). In carbonate environments, shallow platform or reef facies
682 with excellent reservoir potential may be present over salt highs (e.g. Riding 2002; Burgess et al. 2013;
683 Teixell et al. 2017). As salt growth continues, fractures are generated in the overburden, which could form
684 significant secondary porosity within the carbonate reservoirs, increasing quality and producibility (He et
685 al. 2014; Howarth and Alves 2016; Saura et al. 2016).

686
687 Supplementing subsurface data with modelled stratal architectures and depositional facies observations
688 from exhumed halokinetically influenced settings globally (e.g., Banham and Mountney 2013a; 2013b; 2014;
689 Poprawski et al. 2014; 2016; Counts and Amos 2016; Ribes et al. 2015; 2017; Counts et al. 2019;
690 Cumberpatch et al. 2021a) is recommended as a useful workflow for building reservoir models for salt
691 basins with limited data. Observations from multiple-scales and types of models can be combined to further
692 reduce the uncertainty associated with reservoir quality prediction, for example recent finite element
693 modelling (FEM) has shown porosity is lower than expected near the vertical parts of salt structures and
694 higher than expected at the base of diapirs, due to mean principal stress variations (Nikolinakou et al. 2014).

695
696 *Halokinetic zonation*

697 The model results show that a deformation zone exists either side of the diapir in all experiments (Figure
698 4, 5, 6). Outside of this zone, the syn- and pre-kinematic stratigraphy are undeformed (Figure 13). The
699 extent of this salt withdrawal basin is 1150 m on either side of the diapir (2300 m in total). Therefore, the
700 total zone of halokinetic influence in all models is approximately three times the original diapirs' maximum
701 width (750 m), with a deformed zone of 1.5 diapir widths either side of the structure. The width of the
702 deformation zones is comparable across all models (Figure 7), and therefore it is shown that sedimentation
703 rate is unlikely to have a significant control on the width of the zone of halokinetic influence (Giles and
704 Rowan 2012; Hearon et al. 2014). Other factors such as salt supply, salt viscosity, and style and magnitude
705 of regional tectonics (which are not modelled) will in nature, influence the width of the halokinetically
706 deformed zone (Koyi 1998; Fuchs et al. 2011). The model can be further divided into zones based on onlap
707 geometry and thinning rates, which highlight the 'trade off' between reservoir thickness and stratigraphic
708 trap potential in subsurface plays (Figure 13). In the flank locations, bedding dips and thinning rates are
709 shown to be greater under slower sedimentation rates compared to higher sedimentation rates (Figure 8;
710 Table 3), which is important when predicting hydrocarbon column height. Significant overpressures on
711 reservoirs below can be created by fast sedimentation rates (Figure 7; 8; Peeters et al. 2018).

712
713 *Fault distribution*

714 Radial faults associated with salt diapirs are shown to cause compartmentalisation of reservoirs (Birch and
715 Haynes 2003; Scott et al. 2010; Charles and Ryzhikov 2015; Peeters et al. 2018; Coleman et al. 2018). Our
716 DEM replicates localised fault growth, evolution and propagation because the contacts between elements
717 are treated as potential displacement surfaces. Our models all document a similar fault pattern, suggesting
718 that faulting, and therefore fault compartmentalisation is not heavily influenced by sedimentation rate. As
719 well as seismically resolvable faults, outcrop and borehole data indicate brittle deformation is significant in

720 salt basins (e.g. Koestler and Ehrmann 1991; Cumberpatch et al. 2021a). Our DEM replicates this brittle
721 deformation (Figures 4-6); as in nature, extreme thinning, and termination of layers is in part accommodated
722 by small-scale displacements. Understanding sub-seismic scale fault distribution is important for predicting
723 reservoir compartmentalization and seal integrity in the subsurface. Faults, when sealing, could act as lateral
724 permeability barriers, especially if the faults and surrounding reservoir rocks become cemented with salt
725 and salt-related breccia (Van Bergen and de Leeuw 2001; Li et al. 2017). DEM is therefore advantageous in
726 predicting potential traps, conduits and baffles, due to its replication of diapir-related brittle deformation.
727

728 **Future work**

729 The DEM presented here is useful for predicting regional trends and studying generic interactions of salt
730 structures and stratigraphy, but further work is required to recreate specific complicated salt geometries.
731 Other suggestions for further development of this model are to incorporate reactivation and cessation of
732 halokinesis, studying the impact on stratigraphic architectures and the development of halokinetic
733 unconformities. In nature, salt diapirs are rarely isolated structures, and therefore subsequent studies will
734 focus on the interaction of multiple salt structures, with different growth histories on different
735 sedimentary successions. Many of the limitations of the model described above, are due to its two-
736 dimensional nature. The ultimate aim of future work is developing a three-dimensional DEM to better
737 understand the four-dimensional variability in halokinetically-influenced stratigraphy and associated
738 subsurface energy reservoirs.

739 **CONCLUSIONS**

740

741 1) Discrete element modelling (DEM) can form an integral part of the workflow when studying salt-
742 sediment interactions. Here, a DEM is used to study the variability in stratigraphic architecture and
743 deformation patterns, around a growing salt structure under different sedimentation rates.
744

745 2) The models generate realistic salt-related faults. In all models, structural deformation and extent of
746 halokinetic influence are similar, and syn-kinematic strata, at least initially, are isolated to either side
747 of the diapir, thinning and onlapping towards the high.
748

749 3) Under slow sedimentation rate (M2) deposition is restricted to salt withdrawal basins either side of
750 the diapir throughout evolution, while in M3-M6 sedimentation eventually occurs over the diapir
751 crest, often associated with significant lateral thickness variability. Diapir growth is most inhibited
752 under fast aggradation (M4) and the halokinetic influence on stratigraphy reduces quickly with
753 time.
754

755 4) Thinning of syn-kinematic stratigraphy from the undeformed section to the diapir flanks, is greatest
756 under slow aggradation (M2, 34%), and least under fast aggradation (M4, 12%). In all models,
757 thinning is about six times greater between the salt flank and crest, compared to the undeformed
758 section and the salt flank, indicating more intense deformation close to the diapir.
759

760 5) Thinning rate decreases through time (up stratigraphy), showing a reduction of halokinetic
761 modulation with increased sediment thickness, as halokinetic bathymetry is 'healed'. This is true
762 for all models except for decreasing sedimentation (M6), which experiences a slight increase up
763 stratigraphy.
764

765 6) Our simplified two-dimensional models provide useful analogues for salt-influenced basins with
766 complicated four-dimensional evolutions. Natural examples record the interplay between
767 sedimentation rate and diapir rise rate, whilst models isolate and vary sedimentation rate.
768 Comparison to the Pierce field diapirs, North Sea, shows how different models can be applicable
769 to different parts of stratigraphy and suggest how interpreters could infer likely sedimentation rates
770 and conditions from subsurface stratigraphic geometries.
771

772 7) Facies, and thus reservoir distribution, around salt diapirs will differ from unconfined settings due
773 to halokinetic modulation, both vertically and laterally. A deep-water analogue from stratigraphy

774 adjacent to the Bakio diapir, shows that halokinetically influenced facies (e.g., the salt flank) contain
775 thin beds, sandstone pinchouts and increased mass transport deposits in comparison with the
776 allogenic deposits (e.g., the undeformed zone), which are difficult to decipher from deep-water
777 strata in non-salt influenced settings.

778
779 8) Integrating DEM with subsurface and outcrop data helps to reduce reservoir and trap uncertainty
780 in subsurface energy exploration and development.
781

782 **ACKNOWLEDGEMENTS**

783 This paper contains work conducted during ZCs' PhD study undertaken as part of the Natural
784 Environment Research Council (NERC) Centre for Doctoral Training (CDT) in Oil & Gas [grant number
785 NEM00578X/1]. We thank PGS for permission to publish an image extracted from MegaSurvey Plus 3D
786 seismic data.

787 Contribution to the manuscript per author: Writing and figure design: ZC, Model design: EF, LP, ZC
788 conceptualization of models: ZC, EF, IK, LP, CJ, Model analysis and interpretation: ZC, IK, EF, LP, DH,
789 CJ, Seismic interpretation and integration: ZC, BK, IK, DH, MH, CJ, LP, Discussions and Editing: ZC,
790 IK, EF, LP, DH, CJ, BK, MH.

791 **REFERENCES**

792 ABE, S., VAN GENT, H., AND URAI, J.L. (2011) DEM simulation of normal faults in cohesive materials:
793 Tectonophysics v. 512, p. 12-21.

794 ABE, S. AND URAI, J.L. (2012) Discrete element modelling of boudinage: insights on rock rheology,
795 matrix flow, and evolution of geometry: Journal of Geophysical Research. Solid Earth, v. 117.

796 ADAMS, E., AND KENTER, J. (2012) So Different, Yet So Similar: Comparing and Contrasting
797 Siiclastic and Carbonate Slopes: AAPG Search and Discovery Article 50683.

798 ALBERTZ, M., AND INGS, S.J. (2012) Some consequences of mechanical stratification in basin-scale
799 numerical models of passive margin salt tectonics, in Alsop, G.I., Archer, S.G., Hartley, A.J., Grant, N.T.,
800 and Hodgkinson, R., eds., Salt Tectonics, Sediments and Prospectivity: Geological Society, London, Special
801 Publications, v. 363, p. 303-330.

802
803 ALLEN, M.P., AND TILDESLEY, D.J. (1987) Molecular Simulation of Liquids: Clarendon, Oxford. Amy,
804 L.A., McCaffrey, W.D. and Kneller, B.C., 2004, The influence of a lateral basin-slope on the depositional
805 patterns of natural and experimental turbidity currents, *in* Lomas, S.A., and Joseph, P., eds., Confined
806 Turbidite Systems, Geological Society, London, Special Publications. v. 222, p. 311-330.

807 ANDREWS, B.J., CUMBERPATCH, Z.A., SHIPTON, Z.K., AND LORD, R (2020) Collapse processes
808 in abandoned pillar and stall coal mines: Implications for shallow mine geothermal energy: Geothermics, v.
809 88, 101904.

810 BANHAM, S.G., AND MOUNTNEY, N.P. (2013a) Evolution of fluvial systems in salt-walled mini-
811 basins: a review and new insights: Sedimentary Geology, v. 296, p. 142–166.

812
813 BANHAM, S.G., AND MOUNTNEY, N.P. (2013b) Controls on fluvial sedimentary architecture and
814 sediment-fill state in salt-walled mini-basins: Triassic Moenkopi Formation, Salt Anticline Region, SE Utah,
815 USA: Basin Research, v. 25, p. 709–737.

816
817 BANHAM, S.G., AND MOUNTNEY, N.P. (2014) Climatic versus halokinetic control on sedimentation
818 in a dryland fluvial succession: Sedimentology, v. 61, p. 570–608.
819

820 BELHEINE, N., PLASSIARD, J.P., DONZÉ, F. V., DARVE, F., AND SERIDI, A. (2009), Numerical
821 simulation of drained triaxial test using 3D discrete element modeling: *Computers and Geotechnics*, v. 36,
822 p. 320-331.
823

824 BENSEGHIER, Z., CUÉLLAR, P., LUU, L.H., BONELLI, S., AND PHILIPPE, P. (2020) A parallel
825 GPU-based computational framework for the micromechanical analysis of geotechnical and erosion
826 problems: *Computers and Geotechnics*, v. 120, 103404.
827

828 BERTON, F., AND VESELY, F. F. (2016) Seismic expression of depositional elements associated with a
829 strongly progradational shelf margin: northern Santos Basin, southeastern Brazil: *Brazilian Journal of*
830 *Geology*, v. 46(4), p. 585-603.
831

832 BIRCH, P., AND HAYNES, J. (2003) The Pierce Field Blocks 23/22a, 23/27, UK North Sea: Geological
833 Society, London, Memoir 20, p. 618-647.
834

835 BONINI, M. (2003) Detachment folding, fold amplification, and diapirism in thrust wedge experiments:
836 *Tectonics*, v. 22 (6), 1065.
837

838 BOOTH, J. R., DEAN, M. C., DUVERNAY, A. E., AND STYZEN, M. J. (2003) Paleo-bathymetric
839 controls on the stratigraphic architecture and reservoir development of confined fans in the Auger Basin:
840 *Central Gulf of Mexico slope: Marine and Petroleum Geology*, v. 20, p. 563–586.
841

842 BOTTER, C., CARDOZO, N., HARDY, S., LECOMTE, I., AND ESCALONA, A. (2014) From
843 mechanical modelling to seismic imaging of faults: A synthetic workflow to study the impact of faults on
844 seismic: *Marine and Petroleum Geology*, v. 57, p. 187-200.
845

846 BURGESS, P.M., WINEFIELD, P., MINOZONI, M., AND ELDERS, C. (2013) Methods for
847 identification of isolated carbonate buildups from seismic reflection data: *AAPG Bulletin*, v. 97 (7), p. 1071-
848 1098.
849

850 BURGESS, P.M. (2012) A brief review of developments in stratigraphic forward modelling, 2000-2009, *in*
851 Roberts, D.G., and Bally, A.W., eds., *Regional Geology and Tectonics: Principles of Geologic Analysis*, v.
852 1A, Elsevier, p. 864.
853

854 CARRUTHERS, D., CARTWRIGHT, J., JACKSON, M.P.A. AND SCHUTJENS, P. (2013) Origin and
855 timing of layer-bound radial faulting around North Sea salt stocks: New insights into the evolving stress
856 state around rising diapirs: *Marine and Petroleum Geology*, v. 48, p. 130-148.
857

858 CHARLES, R., AND RYZHIKOV, K. (2015) Merganser Field: managing subsurface uncertainty during
859 the development of a salt diapir field in the UK Central North Sea, *in* Mckie, T., Rose, P.T.S., Hartley, A.J.,
860 Jones, D.W. and Armstrong, T.L., eds., *Tertiary Deep-Marine Reservoirs of the North Sea Region*,
861 Geological Society Special Publication, V. 403, 261-298.
862

863 CHEMIA, Z., KOYI, H. AND SCHMELING, H. (2008) Numerical modelling of rise and fall of a dense
864 layer in salt diapirs, *Geophysical Journal International*, v. 172 (2), p. 798–816.
865

866 CIL, M.B., AND ALSHIBLI, K.A. (2012) 3D assessment of fracture of sand particles using discrete
867 element method: *Géotechnique Letters*, v. 2 (3), p. 161-166.
868

869 Coleman, A.J., Jackson, C., A-L., Duffy, O.B., and Nikolinakou, M.A., 2018, How, where, and when do
870 radial faults grow near salt diapirs?: *Geology*, v. 46 (7), p. 655-658.

871

872 COSTA, E., AND VENDEVILLE, B.C. (2002) Experimental insights on the Geometry and Kinematics
873 of Fold-and-Thrust Belts Above Weak, Viscous Evaporitic Décollement: *Journal of Structural Geology*, v.
874 24, p. 1729-1739.

875

876 COUNTS, J.W., AND AMOS, K.J. (2016) Sedimentology, depositional environments and significance of
877 an Ediacaran salt-withdrawal minibasin, Billy Springs Formation, Flinders Ranges, South Australia:
878 *Sedimentology*, v. 63, p. 1084-1123.

879

880 COUNTS, J.W., DALGARNO, C.R., AMOS, K.J., AND HASIOTIS, S.T. (2019) Lateral facies variability
881 along the margin of an outcropping salt-withdrawal minibasin, South Australia: *Journal of Sedimentary*
882 *Research*, v. 89, p. 28-45.

883

884 CUMBERPATCH, Z.A., KANE, I.A., SOUTTER, E.L., HODGSON, D.M., JACKSON, C. A-L.,
885 KILHAMS, B.A., AND POPRAWSKI, Y. (2021a) Interactions of deep-water gravity flows and active salt
886 tectonics, *Journal of Sedimentary Research*.

887

888 CUMBERPATCH, Z.A., FINCH, E., AND KANE, I.A. (2021b) External signal preservation in
889 halokinetic stratigraphy: A Discrete Element Modeling (DEM) approach: *Geology*

890

891 DANIILIDIS, A., AND HERBER, R. (2017) Salt intrusions providing a new geothermal exploration target
892 for higher energy recovery at shallower depths: *Energy*, v. 118, p. 658-670.

893

894 DAVISON, I., INSLEY, M., HARPER, M., WESTON, P., BLUNDELL, D., MCCLAY, K., AND
895 QUALLINGTON, A. (1993) Physical modelling of overburden deformation around salt diapirs:
896 *Tectonophysics*, v. 228, p. 255-274.

897

898 DAVISON, I., ALSOP, I., BIRCH, P., ELDERS, C., EVANS, N., NICHOLSON, H., RORISON, P.,
899 WADE, D., WOODWARD, J., AND YOUNG, M. (2000a) Geometry and late-stage structural evolution
900 of Central Graben salt diapirs, North Sea: *Marine and Petroleum Geology*, v. 17, p. 499-522.

901

902 DAVISON, I., ALSOP, G.I., EVANS, N.G., AND SAFARICZ, M. (2000b) Overburden deformation
903 patterns and mechanisms of salt diapir penetration in the Central Graben, North Sea: *Marine and Petroleum*
904 *Geology*, v. 17, p. 601–618.

905

906 DE HAAS, H., OKKELS, E. AND VAN WEERING, T.C.E. (1996) Recent sediment accumulation in
907 the Norwegian Channel, North Sea. *Norges Geologiske Undersøkelse Bulletin*, v. 430, p. 57-65.

908

909 DEN HARTOG JAGER, D., GILES, M.R., GRIFFITHS, G.R. (1993) Evolution of Paleogene sub-
910 marine fans of the North Sea in space and time. In: Parker, J.R. (Ed.), *Petroleum Geology of Northwest*
911 *Europe: Proceedings of the 4th Conference*, The Geological Society, London, pp. 59-71.

912

913 DONZÉ, F., MORA, P., AND MAGNIER, S-A., (1994) Numerical simulation of faults and shear zones,
914 *Geophysical Journal International*, v. 116, p. 46-52.

915

916 DOOLEY, T.P., AND HUDEC, M.R. (2017) The effects of base-salt relief on salt flow and suprasalt
917 deformation patterns – Part 2: Application to the eastern Gulf of Mexico: *Interpretation*, 5(1) p. 25-38.

- 918 DOOLEY, T.P., JACKSON, M.P., AND HUDEC, M.R., (2009) Inflation and deflation of deeply buried
919 salt stocks during lateral shortening: *Journal of Structural Geology*, v. 31(6), p. 582-600.
- 920 DOOLEY, T.P., HUDEC, M.R., AND JACKSON, M.P. (2012) The structure and evolution of sutures in
921 allochthonous salt: *AAPG Bulletin*, v. 96(6), p. 1045-1070.
- 922 DOOLEY, T.P., JACKSON, M.P.A, AND HUDEC, M.R. (2013) Coeval extension and shortening above
923 and below salt canopies on an uplifted, continental margin: Application to the northern Gulf of Mexico:
924 *AAPG Bulletin*, v. 97(10), p. 1737-1764.
- 925 DOOLEY, T.P., JACKSON, M.P.A., JACKSON, C.A-L., HUDEC, M.R., AND RODRIGUEZ, C.R.,
926 (2015) Engimatic structures within salt walls of the Santos Basin- Part 2: Mechanical explanation from
927 physical modelling: *Journal of Structural Geology*, v. 75, p. 163-187.
- 928 DOOLEY, T.P., HUDEC, M.R., PICHEL, L.M., AND JACKSON, M.P.A. (2020) The impact of base-
929 salt relief on salt flow and suprasalt deformation patterns at the autochthonous, paraautochthonous and
930 allochthonous level: insights from physical models: *Journal of the Geological Society, Special Publications*.
931 v. 476 (2), p. 287-315.
- 932 DOUGHTY-JONES, G., MAYALL, M., AND LONERGAN, L. (2017) Stratigraphy, facies, and evolution
933 of deep-water lobe complexes within a salt controlled intraslope minibasin: *AAPG Bulletin*, v. 101, p. 1879-
934 1904.
- 935
936 DOUGHTY-JONES, G., LONERGAN, L., MAYALL, M., AND DEE, S.J. (2019) The role of structural
937 growth in controlling the facies and distribution of mass transport deposits in a deep-water salt minibasin:
938 *Marine and Petroleum Geology*, v. 104, p. 106-124.
- 939
940 DUFFY, O.B., FERNANDEZ, N., HUDEC, M.R., JACKSON, M.P.A., BURG, G., DOOLEY, T.P.
941 AND JACKSON, C. A-L. (2017) Lateral mobility of minibasins during shortening: Insights from the SE
942 Precaspian Basin, Kazakhstan: *Journal of Structural Geology*, v. 97, p. 257-276.
- 943
944 DUFFY, O.B., DOOLEY, T.P., HUDEC, M.R., JACKSON, M.P.A., FERNANDEZ, N. JACKSON, C,
945 A-L. AND SOTO, J.I. (2018) Structural evolution of salt-influenced fold-and-thrust belts: A synthesis and
946 new insights from basins containing isolated salt diapirs: *Journal of Structural Geology*, v. 114, p. 206-221.
- 947
948 DUTTA, U., BARUAH, A., AND MANDAL, N. (2016) Role of source-layer tilts in the axi-asymmetric
949 growth of diapirs triggered by a Rayleigh-Taylor instability: *Geophysical Journal International*, v. 206, p.
950 1814-1830.
- 951
952 ELDRETT, J., TRIPSANAS, E., DAVIS, C., MCKIE, T., VIERA, M., OSTERLOFF, P. AND
953 SANDISON, T. (2015) Sedimentological evolution of Sele Formation deep-marine depositional systems
954 of the Central North Sea. *Geological Society, London, Special Publications*, 403, 63-98.
- 955
956 FERNANDEZ, N., AND KAUS, B.J.P, (2015) Pattern formation in 3-D numerical models of down-built
957 diapirs initiated by a Rayleigh-Taylor instability: *Geophysical Journal International*, v. 202 (2), p. 1253-
958 1270.
- 959
960 FERNANDEZ, N., HUDEC, M.R., JACKSON, C, A-L., DOOLEY, T.P. AND DUFFY, O.B. (2020)
961 The competition for salt and kinematic interactions between minibasins during density-driven subsidence:
962 observations from numerical models: *Petroleum Geoscience*, v. 26 (1), p. 3-15.
- 963

964 FERRER, O., MCCLAY, K., AND SELLIER, N. C. (2017) Influence of fault geometries and mechanical
965 anisotropies on the growth and inversion of hanging-wall synclinal basins: Insights from sandbox models
966 and natural examples: Geological Society, London, Special Publications, v. 439(1), p. 487–509.
967

968 FINCH, E. (1998); A Crustal Lattice Solid Model: The Evolution, Geometry and Scaling of Tectonic
969 Extension. PhD thesis, School of Environmental Sciences, University of Ulster.
970

971 FINCH, E., HARDY, S., AND GAWTHORPE, R., (2003) Discrete element modelling of contractional
972 fault-propagation folding above rigid basement fault blocks: Journal of Structural Geology, v. 25(4), p. 515–
973 528.
974

975 FINCH, E., HARDY, S., AND GAWTHORPE, R., (2004) Discrete-element modelling of extensional
976 fault-propagation folding above rigid basement fault blocks: Basin Research, v. 16(4), p. 467–488.
977

978 FUCHS, L., SCHMELING, H., AND KOYI, H., (2011) Numerical models of salt diapir formation by
979 down-building: the role of sedimentation rate, viscosity contrast, initial amplitude and wave length:
980 Geophysical Journal International, v. 186, p. 390-400.
981

982 GARCÍA-MONDÉJAR, J., (1996) Plate reconstruction of the Bay of Biscay: Geology, v. 24, p. 635-638.

983 GAULLIER, V., AND VENDEVILLE, B.C., (2005) Salt tectonics driven by sediment progradation: Part
984 II- Radial spreading of sedimentary lobes prograding above salt: AAPG Bulletin, v. 89 (8), p. 1081-1089.
985

986 GEMMER, L., INGS, S.J., MEDVEDEV, S., AND BEAUMONT, C., (2004) Salt tectonics driven by
987 differential sediment loading: stability analysis and finite-element experiments: Basin Research, v. 16, p.
988 199-218.
989

990 GEMMER, L., BEAUMONT, C., INGS, S.J., (2005) Dynamic modelling of passive margin salt tectonics:
991 effects of water loading, sediment properties and sedimentation patterns: Basin Research, v. 17, p. 382-402.
992

993 GILES, K., AND LAWTON, T. (2002) Halokinetic sequence stratigraphy adjacent to the El Papalote
994 diapir, Northeastern Mexico: AAPG Bulletin, v. 86, p. 823-840.
995

996 GILES, K., AND ROWAN, M. (2012) Concepts in halokinetic-sequence deformation and stratigraphy, in
997 Alsop, G.I., Archer, S.G., Hartley, A.J., Grant, N.T., and Hodgkinson, R., eds., Salt Tectonics, Sediments
998 and Prospectivity: Geological Society, London, Special Publications, v. 363, p. 7-31.
999

1000 GRANT, R.J., UNDERHILL, J.R., HERNÁNDEZ-CASADO, J., BARKER, S.M., AND JAMIESON,
1001 R.J. (2019) Upper Permian Zechstein Supergroup carbonate-evaporite platform palaeomorphology in the
1002 UK Southern North Sea: Marine and Petroleum Geology, v. 100, p. 484-518.
1003

1004 GRIMSTAD, S., (2016) Salt tectonics in the central and northeastern Nordkapp Basin, Barents Sea [MS
1005 Thesis]: University of Oslo, Norway, 127 p.
1006

1007 HAMILTON-WRIGHT, J., DEE, S., VON NICOLAI, C., AND JOHNSON, H. (2019) Investigating
1008 controls on salt movement in extensional settings using finite-element modelling: Petroleum Geoscience,
1009 v. 25(3), p. 258-271.
1010

1011 HARDY, S., AND FINCH, E. (2005) Discrete-element modelling of detachment folding: Basin Research,
1012 v. 17(4), p. 507-520.
1013

1014 HARDY, S., AND FINCH, E., (2006) Discrete element modelling of the influence of cover strength on
1015 basement-involved fault-propagation folding: Tectonophysics, v. 415, p. 225-238.
1016

- 1017 HARMS, G.L. (2015) Numerical modelling of salt diapirism and the temperature field during thin-skinned
1018 extension; in search of geothermal and hydrocarbon energy sources. Master's thesis, Utrecht University,
1019 The Netherlands, p. 32.
1020
- 1021 HE, L., ZHAO, L., LI, J., MA, J., LUI, R., WANG, S., AND ZHAO, W. (2014) Complex relationship
1022 between porosity and permeability of carbonate reservoirs and its controlling factors: A case study of
1023 platform facies in Pre-Caspian Basin: *Petroleum Exploration and Development*, v. 41 (2), p. 225-234.
1024
- 1025 HEARON, T.E., ROWAN, M.G., GILES, K.A. AND HART, W.H. (2014) Halokinetic deformation
1026 adjacent to the deepwater Auger diapir, Garden Banks 470, northern Gulf of Mexico: Testing the
1027 applicability of an outcrop-based model using subsurface data: *Interpretation*, v. 2(4).
1028
- 1029 HEIDARI, M., NIKOLINAKOU, M.A., FLEMMINGS, P.B. AND HUDEC, M.R. (2017), A simplified
1030 stress analysis of rising salt domes; *Basin Research*, v. 29 (3), p. 363-376.
1031
- 1032 HEIDARI, M., NIKOLINAKOU, M.A., HUDEC, M.R., AND FLEMMINGS, P.B. (2019) Influence of
1033 a reservoir bed on diapirism and drilling hazards near a salt diapir: a geomechanical approach: *Petroleum*
1034 *Geoscience*, v. 25 (3), p. 282-297.
1035
- 1036 HOSSAIN, S. (2019) Application of seismic attribute analysis in fluvial seismic geomorphology; *Journal of*
1037 *Petroleum Exploration and Production Technology*.
1038
- 1039 HODGSON, N.A., FARNSWORTH, J., AND FRASER, A.J., (1992) Salt-related tectonics, sedimentation
1040 and hydrocarbon plays in the Central Graben, North Sea, UKCS, *in* Hardman, R.F.P., ed., *Exploration*
1041 *Britain: Geological Insights for the Next Decade*, Geological Society, London, Special Publications, v. 67,
1042 p. 31–63.
1043
- 1044 HOWARTH, V., AND ALVES, T.M. (2016) Fluid flow through carbonate platforms as evidence for deep-
1045 seated reservoirs in Northwest Australia: *Marine Geology*, v. 380, p. 17-43.
1046
- 1047 HOWLETT, D.M., GAWTHORPE, R.L., GE, Z., ROTEVATN, A., AND JACKSON, C, A-L., (2020)
1048 Turbidites, topography and tectonics: Evolution of submarine channel-lobe systems in the salt-influenced
1049 Kwanza Basin, offshore Angola: *Basin Research*, online early.
1050
- 1051 HUDEC, M., AND JACKSON, M. (2007) Terra infirma: Understanding salt tectonics: *Earth-Science*
1052 *Reviews*, v. 82, p. 1-28.
1053
- 1054 HUDEC, M.R., AND JACKSON, M.P.A. (2011) *The salt mine: a digital atlas of salt tectonics*: Austin, TX,
1055 the University of Texas at Austin, Bureau of Economic Geology, Udden Book Series 5; Tulsa, OK,
1056 American Association of Petroleum Geologists, Memoir 99, p. 305.
1057
- 1058 HUDEC, M., NORTON, I.O., JACKSON, M.P.A. AND PEEL, F.J. (2013) Jurassic evolution of the Gulf
1059 of Mexico salt basin: *AAPG Bulletin*, v. 97 (10), p. 1638-1710.
1060
- 1061 IMBER, J., TUCKWELL, G.W., CHILDS, C., WALSH, J.J., MANZOCCHI, T., HEATH, A.E.,
1062 BONSON, C.G., AND STRAND, J., (2004), Three-dimensional distinct element modelling of relay growth
1063 and breaching along normal faults: *Journal of Structural Geology*, v. 26, p. 1897–1911.
1064
- 1065 ISMAIL-ZADEH, A.T., TALBOT, C.J. AND VOLOZH, Y.A., (2001) Dynamic restoration of profiles
1066 across diapiric salt structures: numerical approach and its applications: *Tectonophysics*, v. 337, p. 23-38.
1067
- 1068 ISMAIL-ZADEH, A.T., TSEPELEV, I., TALBOT, C. AND KOROTKII, A., (2004) Three-dimensional
1069 forward and backward modelling of diapirism: numerical approach and its applicability to the evolution of

1070 salt structures in the Pricaspian basin: *Tectonophysics*, v. 387, p. 81-103.
1071
1072 JACKSON, M. P. A., AND HUDEC, M. R. (2017) *Salt Tectonics: Principles and Practise*, Cambridge
1073 University Press, p. 515.

1074 JENNETTE, D.C., GARFIELD, T.R., MOHRIG, D.C. AND CAYLEY, G.T., (2000) The interaction of
1075 shelf accommodation, sediment supply and sea level in controlling the facies, architecture and sequence
1076 stacking patterns of the Tay and Forties/Sele basin- floor fans, Central North Sea. In: Weimer, P., Slatt,
1077 R.M., Coleman, J., Rosen, N.C., Nelson, H., Bouma, A.H., Styzen, M.J., Lawrence, D.T. (Eds.), *Deep Water
1078 Reservoirs of the World*. GCSSEPM Foundation 20th Annual Bob F. Perkins Research Conference, pp.
1079 402-421.

1080 JONES, I.F., AND DAVISON, I. (2014) *Seismic imaging in and around salt bodies: Interpretation*. v. 2,
1081 p. 1-20.
1082

1083 KANE, I.A., MCGEE, D.T., AND JOBE, Z.R., (2012) Halokinetic effects on submarine channel
1084 equilibrium profiles and implications for facies architecture: conceptual model illustrated with a case study
1085 from Magnolia Field, Gulf of Mexico: *in* Alsop, G.I., Archer, S.G., Hartley, A.J., Grant, N.T., and
1086 Hodgkinson, R., eds., *Salt Tectonics, Sediments and Prospectivity*: Geological Society, London, Special
1087 Publications, v. 363, p. 289-302.
1088

1089 KATZ, O., MORGAN, J.K., AHARONOV, E., AND DUGAN, B., (2014) Controls on the size and
1090 geometry of landslides: Insights from discrete element numerical simulations: *Geomorphology*, v. 220, p.
1091 104-113.
1092

1093 KOESTLER, A.G., AND EHRMANN, W.U., (1991) Description of brittle extensional features in chalk
1094 on the crest of a salt ridge (NW Germany) in Roberts, A.M., Yielding, G., and Freeman, B., eds., *The
1095 Geometry of Normal Faults*: Geological Society, London, Special Publications, v. 56, p. 113-123.
1096

1097 KOYI, H., (1998) The shaping of salt diapirs: *Journal of Structural Geology*, v. 20, p. 321-338.
1098

1099 KERNEN, R.A., GILES, K.A., ROWAN, M.G., LAWTON, T.F., AND HEARON, T.E., (2012)
1100 Depositional and Halokinetic-Sequence Stratigraphy of the Neoproterozoic Wonoka Formation Adjacent
1101 to Patawarta Allochthonous Salt Sheet, Central Flinders Ranges, South Australia, *in* Alsop, G.I., Archer,
1102 S.G., Hartley, A.J., Grant, N.T., and Hodgkinson, R., eds., *Salt Tectonics, Sediments and Prospectivity*:
1103 Geological Society, London, Special Publications, v. 363, p. 81-105.
1104

1105 KERNEN, R.A., GILES, K.A., POE, P.L., GANNAWAY DALTON, C.E., ROWAN, M.G., FIDUCK,
1106 J.C., AND HEARON, T.E., (2018) Origin of the Neoproterozoic rim dolomite as lateral carbonate
1107 caprock, Patawarta Salt Sheet, Flinders Ranges, South Australia: *Australian Journal of Earth Sciences*.
1108

1109 KILHAMS, B.A., MORTON, A., BORELLA, R., WILKINS, A., AND HURST, A. (2014) Understanding
1110 the provenance and reservoir quality of the Sele Formation sandstones of the UK Central Graben utilizing
1111 detrital garnet suites, *in* Scott, R.A., Smyth, H.R., Morton, A.C., and Richardson, N., eds., *Sediment
1112 Provenance Studies in Hydrocarbon Exploration and Production*: Geological Society, London, Special
1113 Publications, v. 386, p. 129-142.
1114

1115 KNELLER, B.C., AND MCCAFFREY, W.D., (1999) Depositional effects of flow non-uniformity and
1116 stratification within turbidity currents approaching a bounding slope: deflection, reflection and facies
1117 variation: *Journal of Sedimentary Research*, v. 69, p. 980-991.
1118

- 1119 LERCHE, I. AND PETERSEN, K. (1995) Salt and sediment dynamics, London, p. 336.
- 1120 LI, S. Y., AND URAI, J. L., (2016) Rheology of rock salt for salt tectonics modelling: Petroleum Science,
1121 v. 13, p. 712–724.
- 1122 LIU, X., AND GALLOWAY, W.E., (1997) Quantitative determination of tertiary sediment supply to the
1123 North Sea Basin: AAPG Bulletin, v. 81 (9), 1482-1509.
- 1124 LONGSHAW, S.M., TURNER, M.J., FINCH, E., AND GAWTHORPE, R., (2009) Discrete Element
1125 Modelling Using a Parallelised Physics Engine: Theory and Practice of Computer Graphics – Eurographics
1126 UK Chapter Proceedings, p. 207-214.
- 1127 LONGSHAW, S.M., TURNER, M.J., AND FINCH, E., (2012) Visualizing a Spherical Geological Discrete
1128 Element Model of Fault Evolution: Theory and Practice of Computer Graphics – Eurographics UK
1129 Chapter Proceedings, p. 77-84.
- 1130 LU, C-Y., TANG, C-L., CHAN, Y-C., HU, J-C., AND CHI, C-C., (2014) Forecasting landslide hazard by
1131 the 3D discrete element method: A case study of the unstable slope in the Lushan hot spring district, central
1132 Taiwan: Engineering Geology, v. 183, p. 14-30.
- 1133 LUO, G., NIKOLINAKOU, M.A., FLEMINGS, P.B. AND HUDEC, M.R. (2012) Geomechanical
1134 modeling of stresses adjacent to salt bodies: Part 1—Uncoupled models: AAPG Bulletin, v. 96 (1), p. 43–
1135 64.
1136
- 1137 LUO, G., HUDEC, M.R., FLEMMINGS, P.B. AND NIKOLINAKOU, M.A. (2017) Deformation, stress,
1138 and pore pressure in an evolving suprasalt basin: Solid Earth, v. 122 (7), p. 5663-5690.
1139
- 1140 MADOF, A.S., CHRISTIE-BLICK, N., AND ANDERS, M.H., (2009), Stratigraphic controls on a salt-
1141 withdrawal intraslope minibasin, north-central Green Canyon, Gulf of Mexico: Implications for
1142 misinterpreting sea level change: AAPG Bulletin, v. 93, p. 636-561.
1143
- 1144 MAIA DA COSTA, A., V. M DA COSTA, P., D. UDEBHULU, O., CABRAL AZEVEDO, R., F. F.
1145 EBECKEN, N., C. O. MIRANDA, A., M. DE, ESTON, S., DE, TOMI, G., R. MENEGHINI, J.,
1146 NISHIMOTO, K., RUGGIERE, F., MALTA, E., ÉLIS ROCHA FERNANDES, M., BRANDÃO, C.
1147 AND BREDA, A. (2019), Potential of storing gas with high CO₂ content in salt caverns built in ultra-deep
1148 water in Brazil. Greenhouse Gas Science and Technology, v. 9, pp. 79-94.
1149
- 1150 MANNIE, A.S., JACKSON, C. A-L., AND HAMPSON, G.J. (2014) Shallow-marine reservoir
1151 development in extensional diapir-collapse minibasins: An integrated subsurface case study from the Upper
1152 Jurassic of the Cod terrace, Norwegian North Sea: AAPG Bulletin, v. 98, p. 2019-2055.
1153
- 1154 MANNIE, A.S., JACKSON, C. A-L., HAMPSON, G.J. AND FRASER, A.J. (2016) Tectonic controls on
1155 the spatial distribution and stratigraphic architecture of a net-transgressive shallow-marine synrift
1156 succession in a salt-influenced rift basin: Middle to Upper Jurassic, Norwegian Central North Sea: Journal
1157 of the Geological Society, v. 173, p. 901-915.
1158
- 1159 MARTÍN-CHIVELET, J., BREASTEGUI, X., ROSALES, I., VERA, J.A., VILAS, L., CAUS, R.,
1160 GREAFE, K-I, SERGUA, M., PUIG, C., MAS, R., ROBLES, S., FLOQUET, M., QUESADA, S., RUIZ-
1161 ORTIZ, P. A., FREGENAL-MARTINEZ, M.A., SALAS. R., GARCIA, A., MARTIN-ALGARAARA,
1162 A., ARIAS, C., MELENDEZ, N., CHACON, B., MOLINA, J.M., SANZ, J.L., CASTRO, J.M., GARCIA-
1163 HERNANDEZ, M., CARENAS, B., GARCIA-HIBALGOM J., AND ORTEGA, F., (2002) Cretaceous,

- 1164 *in* Gibbons, W., and Moreno, T., eds., *The Geology of Spain*, Geological Society, London, Special
1165 Publications. p. 255-292.
- 1166
- 1167 MATTSON, A.G., ROYHAN GANI, M., ROESLER, T., GANI, N.D., FORD, J.T., (2020), 3D mapping
1168 of intruding salt bodies in the subsurface of the Gulf of Mexico using 3D seismic data: Results in
1169 Geophysical Sciences, v. 1-4.
- 1170
- 1171 MAYALL, M., LONERGAN, L. BOWMN, A., JAMES, S., MILLES, K., PRIMMER, T., POPE, D.
1172 ROGERS, L., AND SKEENE, R., (2010) The response of turbidite slope channels to growth-induced
1173 seabed topography: AAPG Bulletin, v. 94, p. 1011-1030.
- 1174 MORA, P., AND PLACE, D., (1993) A lattice solid model for the nonlinear dynamics of earthquakes:
1175 International Journal of Modern Physics, v. 4, p. 1059-1074.
- 1176 MORA, P., AND PLACE, D., (1994) Simulation of the frictional stick-slip instability: Pure Applied
1177 Geophysics, v. 143, p. 61-87.
- 1178 NIKOLINAKOU, M.A., LUO, G., HUDEC, M.R., AND FLEMINGS, P.B., (2012) Geomechanical
1179 modeling of stresses adjacent to salt bodies: Part 2—Poroelastoplasticity and coupled overpressures: AAPG
1180 Bulletin, v. 96 (1), p. 65–85.
- 1181
- 1182 NIKOLINAKOU, M.A., FLEMMINGS, P.B. AND HUDEC, M.R., (2014), Modelling stress evolution
1183 around a rising diapir: Marine and Petroleum Geology, v. 51, p. 230-238.
- 1184
- 1185 NIKOLINAKOU, M.A., FLEMMINGS, P.B. AND HUDEC, M.R., (2014) Comparison of evolutionary
1186 and static modelling of stresses around a salt diapir: Marine and Petroleum Geology, v. 57, p. 537-545.
- 1187
- 1188 NIKOLINAKOU, M.A., HEIDARI, M., HUDEC, M.R., AND FLEMINGS, P.B., (2017) Initiation and
1189 growth of salt diapirs in tectonically stable settings: Upbuilding and megaflaps: AAPG Bulletin, v. 101 (6),
1190 p. 887–905.
- 1191
- 1192 NIKOLINAKOU, M.A., HEIDARI, M., FLEMMINGS, P.B. AND HUDEC, M.R., (2018)
1193 Geomechanical modelling of pore pressure in evolving salt systems: Marine and Petroleum Geology, v. 93,
1194 p. 272-286.
- 1195
- 1196 OLUBOYO, A.P., GAWTHORPE, R.L., BAKKE, K. AND HADLER-JACOBSEN, F., (2014) Salt
1197 tectonic controls on deep-water turbidite depositional systems: Miocene, southwestern Lower Congo
1198 Basin, offshore Angola: Basin Research, v. 26, p. 597-620.
- 1199
- 1200 ORESKES, N., SHRADER-FRECHETTE, K., AND BELTIX, K., (1994) Verification, Validation, and
1201 Confirmation of Numerical Models in the Earth Sciences: Science, v. 263, p. 641-646.
- 1202
- 1203 PEEL, F.J., (2014) How do salt withdrawal minibasins form? Insights from forward modelling, and
1204 implications for hydrocarbon migration: Tectonophysics, v. 630, p. 222-235.
- 1205
- 1206 PEEL, F.J., HUDEC, M.R., WEIJERMARS, R. (2020) Salt diapir downbuilding: Fast analytical models
1207 based on rates of salt supply and sedimentation: Journal of Structural Geology, online early.
- 1208

- 1209 PEETERS, S. ASSCHERT, A., AND WERWEIJ, H., (2018) Towards a better understanding of the highly
1210 overpressured Lower Triassic Bunter reservoir rocks in the Terschelling Basin. *In*: Kilhams, B., Kulka, P.A.,
1211 Mazur, S., McKie, T., Mijnlief, H.F. and van Ojik, K. (eds) Mesozoic Resource Potential in the Southern
1212 Permian Basin. Geological Society, London, Special Publications, v. 469, p. 223-236.
1213
- 1214 PICHEL, L. M., FINCH, E., HUUSE, M., AND REDFERN, J., (2017) The influence of shortening and
1215 sedimentation on rejuvenation of salt diapirs: A new discrete-element modelling approach: *Journal of*
1216 *Structural Geology*, 104, 61–79.
1217
- 1218 PICHEL, L. M., FINCH, E., AND GAWTHORPE, R.L., (2019) The Impact of Pre-Salt Rift Topography
1219 on Salt Tectonics: A Discrete-Element Modeling Approach: *Tectonics*, v. 38, p. 1466-1488.
1220
- 1221 PICHEL, L.M, AND JACKSON, C. A-L., (2020) Four-dimensional variability of Composite Halokinetic
1222 Sequences: *Basin Research*, online early.
1223
- 1224 POLIAKOV, A.N.B., VAN BELAN, R., PODLADCHIKOV, Y., DAUDRE, B., CLOETINGH, S. AND
1225 TALBOT, C., (1993) Numerical analysis of how sedimentation and redistribution of surficial sediments
1226 affects salt diapirism: *Tectonophysics*, v. 226, p. 199-216.
1227
- 1228 POPRAWSKI, Y., BASILE, C., AGRIRREZABALA, L. M., JAILLARD, E., GAUDIN, M., AND
1229 JACQUIN, T. (2014) Sedimentary and structural record of the Albian growth of the Bakio salt diapir (the
1230 Basque Country, northern Spain): *Basin Research*, v. 26, p. 746-766.
1231
- 1232 POPRAWSKI, Y., BASILE, C., JAILLARD, E., GAUDIN, M., AND LOPEZ, M. (2016) Halokinetic
1233 sequences in carbonate systems: An example from the Middle Albian Bakio Breccias Formation (Basque
1234 Country, Spain): *Sedimentary Geology*, v. 334, p. 34-52.
1235
- 1236 PRATSON, L.F., AND RYAN, W.B.F., (1994) Pliocene to recent infilling and subsidence of intraslope
1237 basins offshore Louisiana: *American Association of Petroleum Geologists Bulletin*, v. 78, p. 1483–1506.
1238
- 1239 PRÉLAT, A., HODGSON, D.M. AND FLINT, S.S., (2009) Evolution, architecture and hierarchy of
1240 distributary deep-water deposits: a high-resolution outcrop investigation from the Permian Karoo Basin,
1241 South Africa: *Sedimentology*, v. 56, p. 2132-2154.
1242
- 1243 PUELLES, P., ÁBALOS, B., GARCÍA DE MADINABEITIA, S., SÁNCHEZ-LORDA, M.E.,
1244 FERNÁNDEZ-ARMAS, S., AND GIL IBARGUCHI, J.I., (2014) Provenance of quartz-rich metamorphic
1245 tectonite pebbles from the ‘Black Flysch’ (W Pyrenees, N Spain): An EBSD and detrital zircon LA-ICP-
1246 MS study: *Tectonophysics*, v. 632, p. 123-137.
1247
- 1248 RIBES, C., KERGARAVAT C, BONNEL, C., CRUMEYROLLE, P., CALLOT, J-P., POISSON, A.,
1249 TEMIZ, H., AND RINGENBACH, J-C., (2015) Fluvial sedimentation in a salt-controlled mini-basin:
1250 Stratal patterns and facies assemblages, Sivas Basin, Turkey: *Sedimentology*, v. 62, p. 1513-1545.
1251
- 1252 RIBES, C., KERGARAVAT, C., CRUMEYROLLE, P., LOPEZ, M., BONNEL, C., POISSON, A.,
1253 KAVAK, K, S., CALLOT, J-C., AND RINGENBACH, J-C., (2017) Factors controlling stratal pattern and
1254 facies distribution of fluvio-lacustrine sedimentation in the Sivas mini-basins, Oligocene (Turkey): *Basin*
1255 *Research*, v. 29 (S1), p. 596-621.
1256
- 1257 RIDER, M., AND KENNEDY, M., (2018) *The Geological Interpretation of Well logs*: Glasgow, Bell and
1258 Ball, 432 p.
1259

- 1260 RIDING, R., (2002) Structure and composition of organic reefs and carbonate mud mounds: concepts and
1261 categories: *Earth-Science Reviews*, v. 58, p. 163-231.
1262
- 1263 ROELOFSE, C., ALVES, T.M., GAFFEIRA, J. AND OMOSANYA, K.O., (2019) An integrated geological
1264 and GIS-based method to assess caprock risk in mature basins proposed for carbon capture and storage:
1265 *International Journal of Greenhouse Gas Control*, v. 80, p. 103-122.
1266
- 1267 RODRIGUEZ, C.R., JACKSON, C.A-L., ROTEVATN, A., BELL, R.E., AND FRANCIS, M., (2018)
1268 Dual tectonic-climatic controls on salt giant deposition in the Santos Basin, offshore Brazil: *GEOSPHERE*,
1269 v. 14, p. 215-242.
1270
- 1271 RODRIGUEZ, C.R., JACKSON, C.A-L., BELL, R.E., ROTEVATN, A. AND FRANCIS, M., (2020)
1272 Deep-water reservoir distribution on a salt-influenced slope, Santos Basin, offshore Brazil: *AAPG Bulletin*,
1273 online early.
1274
- 1275 ROMA, M., FERRER, O., ROCA, E., PLA, O., ESCOSA, F.O. AND BUTILLÉ, M., (2018) Formation
1276 and inversion of salt-detached ramp-syncline basins. Results from analog modeling and application to the
1277 Columbrets Basin (Western Mediterranean): *Tectonophysics*, v. 745, p. 214-228.
1278
- 1279 ROWAN, M.G., LAWTON, T.F., GILES, K.A. AND RATLIFF, R.A., (2003), Near-salt deformation in
1280 La Popa basin, Mexico, and the northern Gulf of Mexico: A general model for passive diapirism: *AAPG*
1281 *Bulletin*, v.87 (5), 733-756.
1282
- 1283 SADLER, P., (1981) Sediment Accumulation Rates and the completeness of Stratigraphic Sections: *The*
1284 *Journal of Geology*, v. 89 (5), p. 569-584.
1285
- 1286 SAURA, E., ARDÈVOL I ORÓ, L., TEIXELL, A. AND VERGÉS, J., (2016) Rising and falling diapirs,
1287 shifting depocenters, and flap overturning in the Cretaceous Sopeira and Sant Gervàs subbasins (Ribagorça
1288 Basin, southern Pyrenees): *Tectonics*, v. 35, p. 638–662.
1289
- 1290 SCOTT, E.D., GELIN, F., JOLLEY, S.J., LEENARTIS, E., SADLER, S.P., AND ELSINGER, R.J.,
1291 (2010), Sedimentological control of fluid flow in deep marine turbidite reservoirs: Pierce Field, UK Central
1292 North Sea, *in*: Jolley, S. J., Fisher, Q. J., Ainsworth, R. B., Vrolijk, P. J., and Delisle, S., (eds) *Reservoir*
1293 *Compartmentalization*. Geological Society, London, Special Publications, v. 347, p. 113–132.
- 1294 SCHÖPFER, M.P.J., CHILDS, C. AND WALSH, J.J., (2006) Localisation of normal faults in multilayer
1295 sequences: *Journal of Structural Geology*, v. 28. P. 816-833.
- 1296 SCHULTZ-ELA, D.D., JACKSON, M.P.A., AND VENDEVILLE, B.C., (1993) Mechanics of active salt
1297 diapirism: *Tectonophysics*, v. 228, p. 275-312.
- 1298 SELLIER, N., AND VENDEVILLE, B.C., (2009) Gravitational Salt Tectonics Triggered by Deposition
1299 of Turbiditic Lobes: a New Experimental Modeling Approach with Applications to Salt Tongues in the
1300 U.S. Gulf of Mexico: *AAPG Search and Discovery Article #40478*.
- 1301 SPENCE, G.H., AND FINCH, E., (2014), Influences of nodular chert rhythmites on natural fracture
1302 networks in carbonates: an outcrop and two-dimensional discrete element modelling study: *Geological*
1303 *Society, London, Special Publications*, v. 374, p. 211-249.
- 1304 SPIERS, C. J., SCHUTJENS, P. M. T. M., BRZESOWSKY, R. H., PEACH, C. J., LIEZENBERG, J. L.,
1305 AND ZWART, H. J., (1990), Experimental determination of constitutive parameters governing creep of
1306 rocksalt by pressure solution: *Geological Society, London, Special Publications*, v. 54, 215–227.

- 1307 SOUTTER, E.L., KANE, I.A., FUHRMANN, A., CUMBERPATCH, Z.A., AND HUUSE, M., (2019),
1308 The Stratigraphic Evolution of Onlap in Clastic Deep-Water Systems: Autogenic Modulation of Allogenic
1309 Signals: *Journal of Sedimentary Research*, v. 89 (10), p. 890-917.
1310
- 1311 SOUTTER, E.L., BELL, D., CUMBERPATCH, Z.A., FERGUSON, R.A., KANE, I.A., SPYCHALA,
1312 Y.T., AND EGGENHUISEN, J. (2021) The effect of topographic orientation on confined turbidity
1313 currents and their deposits. *Frontiers in Earth Science*.
1314
- 1315 STRICKER, S., JONES, S.J., MEADOWS, N. AND BOWEN, L., (2018) Reservoir quality of fluvial
1316 sandstone reservoirs in salt-walled mini-basins: an example from the Seagull field, Central Graben, North
1317 Sea, UK: *Petroleum Science*, v. 15, p. 1–27.
1318
- 1319 SYLVESTER, Z., DEPTUCK, M.E., PRATHER, B.E., PRIMEZ, C., AND O'BYRNE, C., (2012) Seismic
1320 Stratigraphy of a Shelf-Edge Delta and Linked Submarine Channels in the Northeastern Gulf of Mexico:
1321 SEPM Special Publication, v. 99, p. 31-59.
1322
- 1323 SYLVESTER, Z., CANTELLI, A. AND PIRMEZ, C. (2015) Stratigraphic evolution of intraslope
1324 minibasins: Insights from surface-based model: *AAPG Bulletin*, v. 99, p. 1099-1129.
1325
- 1326 TEIXELL, A., BARNALOS, A., ROSALES, I. AND ARBOLEYA, M-L., (2017) Structural and facies
1327 architecture of a diapir-related carbonate minibasin (lower and middle Jurassic, High Atlas, Morocco):
1328 *Marine and Petroleum Geology*, v. 81, p. 334-360.
1329
- 1330 TENZER, R., AND GLADKIKH, V., (2014) Assessment of Density Variations of Marine Sediments with
1331 Ocean and Sediment Depths: *The Scientific World Journal*. Article ID 823296.
1332
- 1333 THOENI, K., GIACOMINI, A., LAMBERT, C., SLOAN, S.W. AND CARTER, J.P., (2014) A 3D
1334 discrete element modelling approach for rockfall analysis with drapery systems: *International Journal of*
1335 *Rock Mechanics and Mining Sciences*, v. 68, p. 107-119.
1336
- 1337 TRUSHEIM, F., (1960) Mechanism of Salt Migration in Northern Germany: *AAPG Bulletin* v. 44, pp.
1338 1519-1540.
1339
- 1340 VAN BERGEN, F., AND DE LEEUW, C.S., (2001) Salt Cementation of Reservoir Rocks near Salt
1341 Domes in the Netherlands North Sea Area – a new Mechanism: *Conference Proceedings, 63rd EAGE*
1342 *Conference and Exhibition, June 2001*.
1343
- 1344 VENDEVILLE, B. C., AND M. P. A. JACKSON, (1992) The rise of diapirs during thin-skinned extension:
1345 *Marine and Petroleum Geology*, v. 9, p. 331-353.
- 1346 VENDEVILLE, B.C., GE, H., AND JACKSON, M.P.A., (1995) Scale models of salt tectonics during
1347 basement-involved extension: *Petroleum Geoscience*, v. 1, p. 179-183.
- 1348 Wang, X., Luthi, S.M., Hodgson, D.M., Sokoutis, D., Willingshofer, E., Groenenberg, R.M., (2017)
1349 Turbidite stacking patterns in salt-controlled minibasins: Insights from integrated analogue models and
1350 numerical fluid flow simulations, *Sedimentology*, v. 64, pp.530-552.
1351
- 1352 WARREN, J., (1999) *Evaporites: Their evolution and economics*: Oxford, Blackwell Science, 438 p.
- 1353 WARREN, J., (2006) *Evaporites: Sediments, resources, and hydrocarbons*: Berlin, Springer, 1035 p.
1354
- 1355 WARREN, J., (2016) *Evaporites: A Geological Compendium*: New York, Springer, 1813 p.
1356

- 1357 WHITMAN, J.M., AND DAVIES, T.A., (1979) Cenozoic oceanic sedimentation rates: how good are the
 1358 data?: *Marine Geology*, v. 30, p. 269-284.
 1359
- 1360 WU, N., JACKSON, C.A-L., JOHNSON, H.D., HODGSON, D.M., AND NUGRAHA, H.D., (2020),
 1361 Mass-transport complexes (MTCs) document subsidence patterns in a northern Gulf of Mexico salt
 1362 minibasin: *Basin Research*, v. 32 (6), p. 1300-1327.
 1363
- 1364 ZHAO, J.J., XIAO, J.G., LEE, M.L. AND MA, Y.T., (2016) Discrete element modelling of a mining-
 1365 induced rock slide: *SpringerPlus*, v. 5, Article number 1633.
- 1366 ZHU, H.P., ZHOU, Z.Y., YANG, R.Y., AND YU, A.B. (2008) Discrete particle simulation of particulate
 1367 systems: A review of major applications and findings: *Chemical Engineering Science*, v. 63, p. 5728-5770.

1368 **FIGURE CAPTIONS**

1369

1370 **Figure 1:** Seismic reflection cross-section from the Pierce diapirs, Eastern Central Graben, UK North Sea
 1371 (located in Figure 10) highlighting some of the key questions and uncertainties of subsurface interpretation
 1372 in salt-influenced basins. Mapping top salt, visualizing pinch-outs and onlap geometries in areas of lower-
 1373 quality data adjacent to the salt (1), confidently mapping top salt (2) and studying the lateral and vertical
 1374 extent of syn-kinematic deformation and sedimentation (3), are challenging. Seismic data courtesy of PGS
 1375 (MegaSurvey Plus 3D seismic data).
 1376

1377 **Figure 2:** Initial set up of the DEM ($T=0$) and key parameters. Initial geometry and rise rates taken from
 1378 North Pierce (Davison et al. 2000). See text for discussion and Table 1 and Supplementary Table 1 for
 1379 further details.
 1380

1381 **Figure 3:** Model 3, the intermediate aggradation experiment with a sedimentation rate of 0.3mm/year.
 1382 Diapir growth rate is continuous and constant throughout (0.023 mm/year). Outputs begin at the start of
 1383 the experiment during a stage of no sedimentation ($T=0$ Myr, circle S0 (sedimentation stage 0)). At $T=2.2$
 1384 Myr (B) the diapir has generated surface topography and sedimentation begins to be added (S0/S1).
 1385 Subsequent outputs are generated at 0.4 Myr intervals across the three equal stages of sedimentation (open
 1386 circles S1-S3) from 2.2 to 4.6 Myr. Active sediment input is constant in stages 1-3 and the boundaries are
 1387 highlighted by the grey circle (e.g. $T=3$ Myr represents the end of sedimentation 1 and the beginning of
 1388 sedimentation event 2). The final output is at 4.6 Myr (H), following the final sedimentation from S3. Due
 1389 to minimal deformation in the outer section of all models, for clarity, subsequent figures will focus on only
 1390 the central 3000 m around the diapir (shown by the grey outline, $T=4.6$ Myr). Subsequent figures are shown
 1391 at $T=4.6$ (H).
 1392

1393 **Figure 4:** M1, the model with no sedimentary fill, after 4.6 Myr. Displayed outputs represent the central
 1394 3000 m of the original output model (located in Figure 3). A) Model output, uninterpreted, pre-kinematic
 1395 layers are numbered for clarity, and ease of subsequent discussion. B) Static image of element displacement
 1396 relative to initial neighbours for M1 after 4.6 Myr (provided for M1-M6 in Supplementary Figure 2). Cold
 1397 colours represent elements that are in contact with their original neighbour and hot colours indicate high
 1398 displacement. This is used to show discontinuities and is a proxy for fault location. C) (A) overlain with (B),
 1399 interpreted with locations of discontinuities, highlighting the methodology used to interpret structures for
 1400 all models. Note how the majority of the internal salt has remained in connection with its original
 1401 neighbouring element and the radial faults are associated with salt withdrawal. The maximum displacement
 1402 shows the relative movement of the salt, the neighbouring overburden, and the high mobility of layers in
 1403 close proximity to the diapir. Note the lack of deformation outside of the salt withdrawal basin. D)
 1404 Interpreted static DEM for 4.6 Myr, faults are taken from discontinuities in (C), and overlain onto (A).
 1405

1406 **Figure 5:** Uninterpreted and interpreted static images of the DEM for M2-M4 (constant sedimentation
 1407 rate models) after 4.6 Myr. A) Uninterpreted models, sedimentary layers are coloured and assigned letters
 1408 for easier discussion. Crest, flank and undeformed labels for M2 reflect the locations of thickness
 1409 measurements taken to calculate thinning rates, this location is consistent across all models (M2-M6), B)
 1410 Interpreted versions of each model. Fault interpretations use displacement from initial neighbour

1411 methodology (see Figure 4, Supplementary Figure 2). Interpretations highlight the width of salt withdrawal
1412 basins (deformed zones), height of diapirs, fault and fracture distributions, stratigraphic thickness variation
1413 and variable halokinetic influence vertically and laterally, discussed in text.

1414

1415 **Figure 6:** Uninterpreted and interpreted static image of the DEM with variable sedimentation (M5 and
1416 M6) after 4.6 Myr. Displayed output represent the central 3000 m of the original output model (located in
1417 Figure 3). A) Uninterpreted models, sedimentary layers are coloured and assigned letters for easier
1418 discussion. Crest, flank and undeformed zones mentioned in text reflect those shown in M2 (Figure 5). B)
1419 Interpreted versions of each model. Fault interpretations use displacement from initial neighbour
1420 methodology (see Figure 4, Supplementary Figure 2). Interpretations highlight the width of salt withdrawal
1421 basins (deformed zones), height of diapirs, fault and fracture distributions, stratigraphic thickness variation
1422 and variable halokinetic influence vertically and laterally discussed in text.

1423

1424 **Figure 7:** Diagrammatic comparison of static 4.6 Myr DEM across all models. Comparison between top
1425 salt (solid line), top of the overburden (dashed line) and top of the sediment (dotted line). The top of
1426 sediment is not shown in M1 as none is added. All cases have a similar top salt outside the deformed zone
1427 (shown by a bold black line). Diapir growth and width of the pre-kinematic overburden anticline are
1428 reduced in M2-M6 when compared to M1 due to overpressure caused by sedimentation (see Table 2). Grey
1429 lines indicate 200 metre divisions vertically. Located on Figure 3.

1430

1431 **Figure 8:** Comparison of stratigraphic thickness for flank location across all models with sediment (M2-
1432 M6) see Figure 5 for location of flank profile. Thicknesses and bedding orientation highlighted. The flank
1433 location shows the most deformation in all models, greatest modulation is observed in M2, and least
1434 modulation is observed in M4, generally modulation decreases upwards, however in M6 bed dip increases
1435 in layers K and L. Models give an indication of the sedimentary thickness and bed rotation expected
1436 adjacent to salt diapirs under different sedimentation rates, aiding prediction of sediment thickness and bed
1437 rotation in the subsurface salt sediment interface.

1438

1439 **Figure 9:** Schematic interpretations of M2-M6, focussed on the central 2000 m of the syn-kinematic
1440 stratigraphy, located in Figure 3. Bullet points highlight the key observations specific to each modelled
1441 scenario. Crestal faults are simplified from Figures 4 -6 to better visualise syn-kinematic stratigraphy.

1442

1443 **Figure 10:** Tectonic framework of the North Sea rift system, and structural map of the Central Graben
1444 showing the location of salt diapirs related to major basin faults and Jurassic salt withdrawal basins
1445 (Carruthers et al. 2013). Red box locates subsurface analogue used for comparison to models and green line
1446 locates Figure 11.

1447

1448 **Figure 11:** Subsurface example of model application comparing some of the modelled results to
1449 stratigraphy from the Pierce Field, Eastern Central Graben, UK North Sea. A,B & D) Models 2, 3 and 5
1450 which are analogous to different parts of the stratigraphy around the Pierce diapirs. C) Interpreted time-
1451 migrated seismic profile across the Pierce diapirs. S1, S2, S3 highlight the likely sequences for comparison
1452 to models. The colour of the text represents which model those packages could represent (e.g. red
1453 represents M5). The location of the undeformed, flank and crest stratigraphic locations used for thinning
1454 rate calculations are shown for north Pierce, and are the same spacing as those used for model calculations
1455 (Figure 5; Table 3). Seismic data courtesy of PGS (MegaSurvey Plus 3D seismic data) from Cumberpatch
1456 et al. 2021b.

1457 **Figure 12:** Conceptual facies diagram for a deep-water succession based on integration of field-based facies
1458 analysis around the Bakio diapir, Basque Cantabrian Basin Northern Spain (see Cumberpatch et al. 2021a
1459 for summary), and the result of M5. A) Deep-water facies interpretation (based on field facies analysis) for
1460 the upper part of the increasing sedimentation model (located on Figure 6). H and A are theoretical
1461 stratigraphic profiles in the halokinetically-influenced and non-halokinetically-influenced zones
1462 respectively. B) Location map of the field analogue, for a full geological discussion see Cumberpatch et al.
1463 in 2021a). C) Outcropping Triassic evaporites on Bakio Beach, believed to be part of the Bakio Diapir. D)
1464 Non-halokinetic succession showing a classic progradational deep-water system (controlled by allogenic
1465 and autogenic processes), accompanied by an example of non-halokinetically influenced strata from the

1466 field. E) Halokinetic stratigraphic profile showing a thinner, modulated succession which is rich in MTDs,
1467 accompanied by a field analogue of an outcrop-scale bed pinch-out and an overlying MTD.

1468

1469 **Figure 13:** Halokinetic zonation scheme shown for M3. The model is divided into 5 zones, 4 of which
1470 experience some form of halokinetic influence. Minimal deformation zones 1 and all stratigraphy outside
1471 of it show virtually no modulation by salt diapirism. Halokinetic influence increases towards the diapir-
1472 cored high, and changes from thinning in the ‘halokinetic’ zone to onlap and abrupt pinch out in the ‘onlap’
1473 and ‘salt flank’ zones. Thinned and reduced stratigraphy are observed over the diapirs crest. The table
1474 highlights that while stratigraphic trap quality may be greater closer to the diapir, reservoir thickness and
1475 quality are likely higher further from the diapir, showing a ‘trade-off’ exists for subsurface energy
1476 exploration and production. Similar zonation is possible for all models.

1478 **TABLE CAPTIONS**

1479 **Table 1:** Details of the different sedimentation patterns and rates used in the six experiments. S1-3 refer to
1480 sedimentation intervals.

1481

1482 **Table 2:** Comparison of diapir growth and overburden anticline width across all six experiments at $T=4.6$
1483 Myr. Measurements are taken from model simulations (Figure 4, 5 and 6). Initial diapir height (1050 m at
1484 $T=0$ Myr) is subtracted from final diapir height to give diapir growth. M2-6 are compared to M1 to show
1485 the percentage reduction that occurs when different amounts of sediment are added. Pre-kinematic anticline
1486 measurements are taken from the stratal termination of layer A, in M1 they are taken from the top of the
1487 overburden at the location of the greatest change in dip. For M2-M6 the width of the overburden is
1488 compared to M1 to show the percentage reduction in overburden anticline width that occurs when different
1489 amounts of sediment are added. Syn-kinematic folded roof measurement are taken from location of greatest
1490 dip change in layer F (Supplementary Figure 1). Value only calculated where layers extend across the entire
1491 structure (M3-M6). Ratio of syn- to pre-kinematic folded roof thickness is calculated.

1492

1493 **Table 3:** Comparison of stratigraphic thinning across M2-M6. Bold headings indicate each model and show
1494 the total thinning for all stratigraphy, beneath each heading this is divided by sedimentary package. Layer
1495 A is excluded as it fills to base level in all models. Layers are subdivided based on observational differences
1496 (e.g. lateral extent across the model) and are broadly grouped into their sedimentation stage (S1, S2, S3).
1497 Percentage thinning and normalised thinning rates (%/m) are shown for U-C (Undeformed to Crest, i.e.,
1498 the total model), U-F (Undeformed to Salt Flank) and F-C (Salt Flank to Crest). In layers which do not
1499 extend across the entire model no results exist for U-C and F-C. The final column displays the ratio of the
1500 normalised thinning rate between the Undeformed to Salt Flank and the Salt Flank to Crest sections, to
1501 show how much more thinning is observed adjacent to the diapir. Locations of undeformed, flank and
1502 crest measurements are shown on Figure 5, and are the same for all models to ensure direct comparison.
1503

1504 **SUPPLEMENTARY MATERIAL**

1505 **Supplementary Figure 1:** Explanation of diapir growth, syn-kinematic folded roof and pre-kinematic
1506 folded roof measurements shown in Table 2, and described within the text. Diagram is based on M3, and
1507 terms are consistent across all models.
1508

1509 **Supplementary Figure 2:** Static image of element displacement relative to initial neighbours for all
1510 models at 4.6 Myr. Cold colours represent elements that are in contact with their original neighbour and
1511 hot colours suggest high displacement. This is used to show discontinuities and is a proxy for fault
1512 location. Note how the majority of the internal salt has remained in connection with its original
1513 neighbouring element, and the radial faults associated with salt withdrawal. The maximum displacement
1514 shows the relative movement of the salt to the neighbouring overburden and the high mobility of layers
1515 in close proximity to the diapir. An apparent lack of deformation is observed outside of the
1516 halokinetically deformed zone. Deformation in sediment is shown over the crest and in the flank region
1517 of each model (see Figure 5 for locations of these areas). Outside of these areas, less deformation is
1518 observed in the overburden, suggesting neighbours have remained in contact and overall packages have
1519 been rotated (consistent with bedding). Displacements relative to initial neighbour in the sedimentary
1520 sequence appear lower than the pre-kinematic overburden, because the overburden has been deforming
1521 for 4.6 Myr, while the sediment has only been deforming for 2.4 Myr. See Spence and Finch (2014) for
1522 further details on relative displacement from initial neighbour.
1523

1524 **Supplementary Table 1:** Summary of geological and mechanical parameter values used in the DEM in
1525 this study and a justification for their use.
1526

1527 **Supplementary Table 2:** Comparison of stratigraphic thinning across different stratigraphy approaching
1528 north Pierce diapir (Figure 11). Packages are compared to a specific sedimentation event in a specific
1529 model, e.g., the Mid-Miocene – Pleistocene is perhaps analogous to the final sedimentary sequence (S3) in
1530 the increasing sedimentation model. Percentage thinning and normalised thinning rates (%/m) are shown

1531 for U-C (Undeformed to Crest), U-F (Undeformed to Salt Flank) and F-C (Salt Flank to Crest). The
1532 positions of the U, F, and C stratigraphic profiles are spaced at the same distance as in modelled examples
1533 (Figure 5). In layers which do not extend across the entire model no results exist for U-C and F-C. An
1534 average seismic velocity of 2000 m/s was used for approximate depth conversion of the time-migrated
1535 seismic data for thinning rate calculations, we are aware this is an over simplification of seismic velocity,
1536 which varies with depth and lithology however it is suitable to give a comparison to modelled values.
1537 Colours subdivide different stratigraphy, and relate to Figure 11.

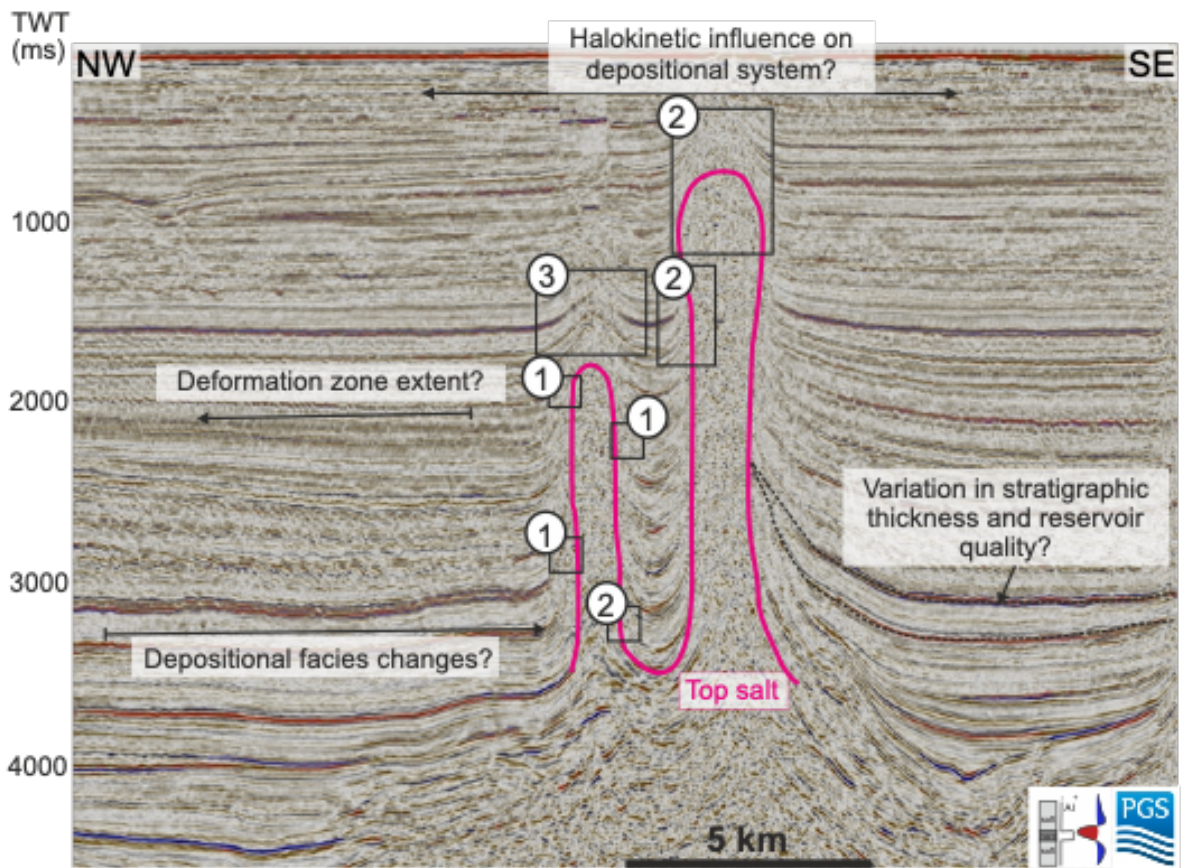


Figure 1: Seismic reflection cross-section from the Pierce diapirs, Eastern Central Graben, UK North Sea (located in Figure 10) highlighting some of the key questions and uncertainties of subsurface interpretation in salt-influenced basins. Mapping top salt, Visualizing pinch-outs and onlap geometries in areas of lower-quality data adjacent to the salt (1), confidently mapping top salt (2) and studying the lateral and vertical extent of syn-kinematic deformation and sedimentation (3), are challenging. Seismic data courtesy of PGS (MegaSurvey Plus 3D seismic data).

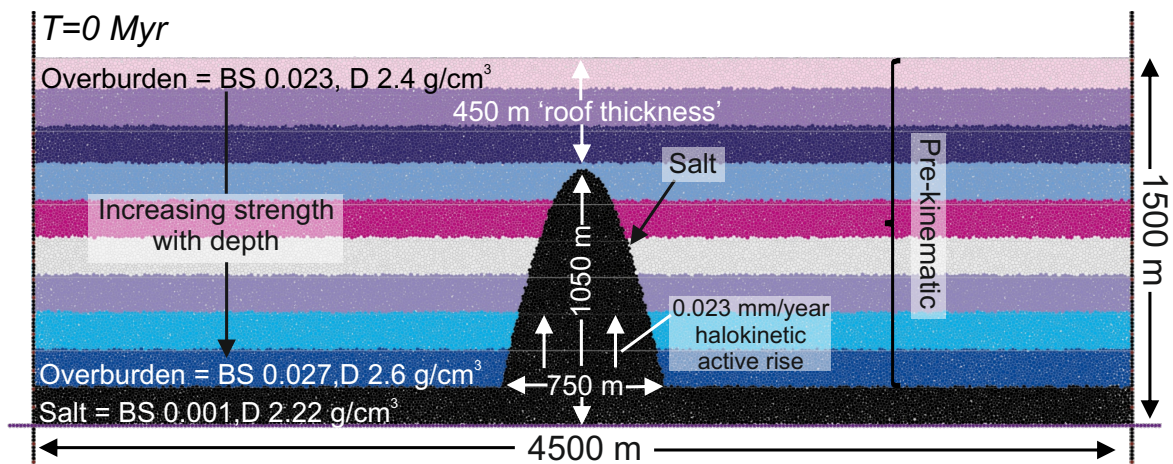


Figure 2: Initial set up of the DEM ($T=0$) and key parameters. Initial geometry and rise rates taken from North Pierce (Davison et al. 2000). See text for discussion and Table 1 and Supplementary Table 1 for further details.

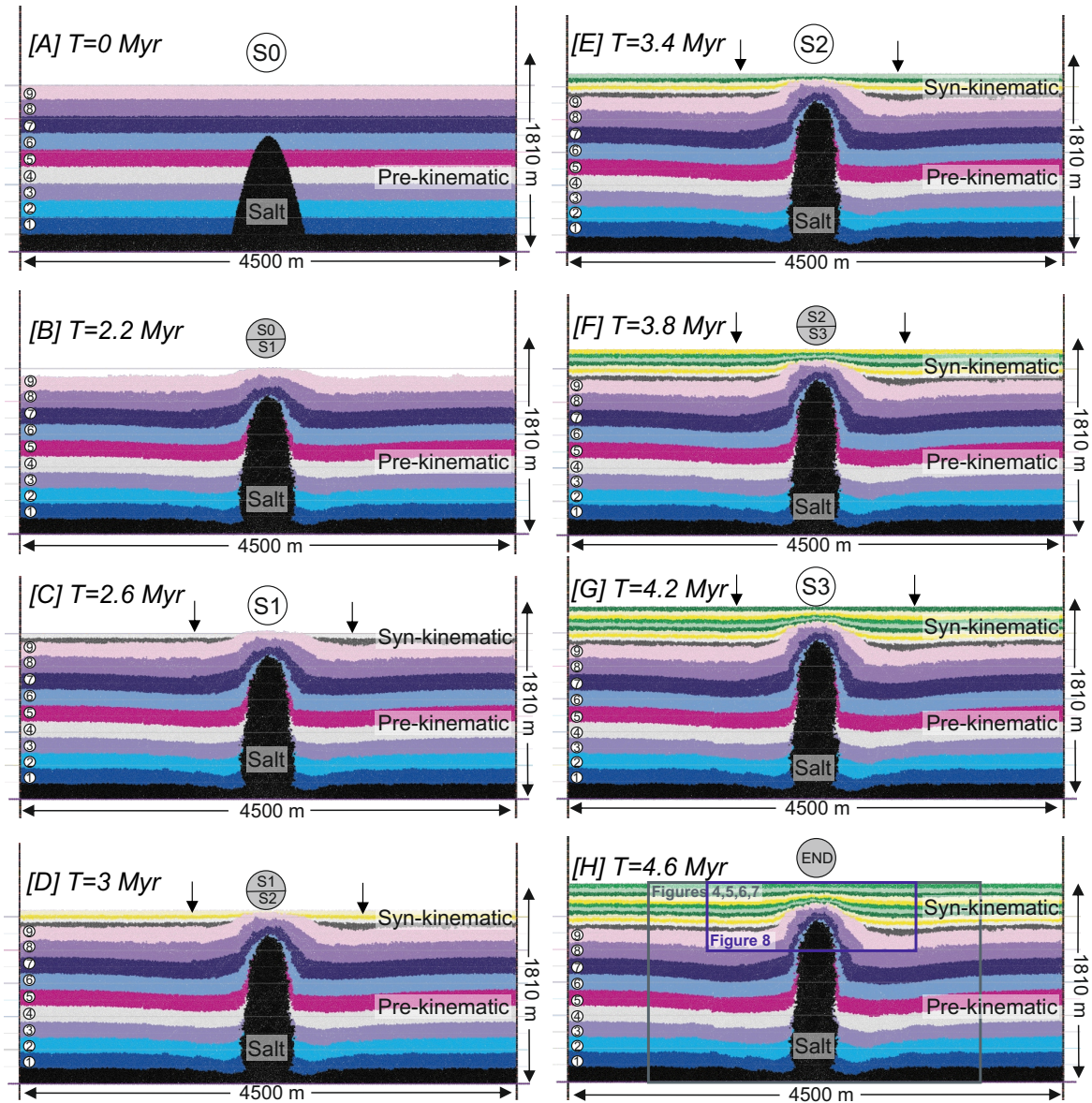


Figure 3: Model 3, the intermediate aggradation experiment with a sedimentation rate of 0.3mm/year. Diapir growth rate is continuous and constant throughout (0.023 mm/year). Outputs begin at the start of the experiment during a stage of no sedimentation ($T=0$ Myr, circle S0 (sedimentation stage 0)). At $T=2.2$ Myr (B) the diapir has generated surface topography and sedimentation begins to be added (S0/S1). Subsequent outputs are generated at 0.4 Myr intervals across the three equal stages of sedimentation (open circles S1-S3) from 2.2 to 4.6 Myr. Active sediment input is constant in stages 1-3 and the boundaries are highlighted by the grey circle (e.g. $T=3$ Myr represents the end of sedimentation 1 and the beginning of sedimentation event 2). The final output is at 4.6 Myr (H), following the final sedimentation from S3. Due to minimal deformation in the outer section of all models, for clarity, subsequent figures will focus on only the central 3000 m around the diapir (shown by the grey outline, $T=4.6$ Myr). Subsequent figures are shown at $T=4.6$ (H).

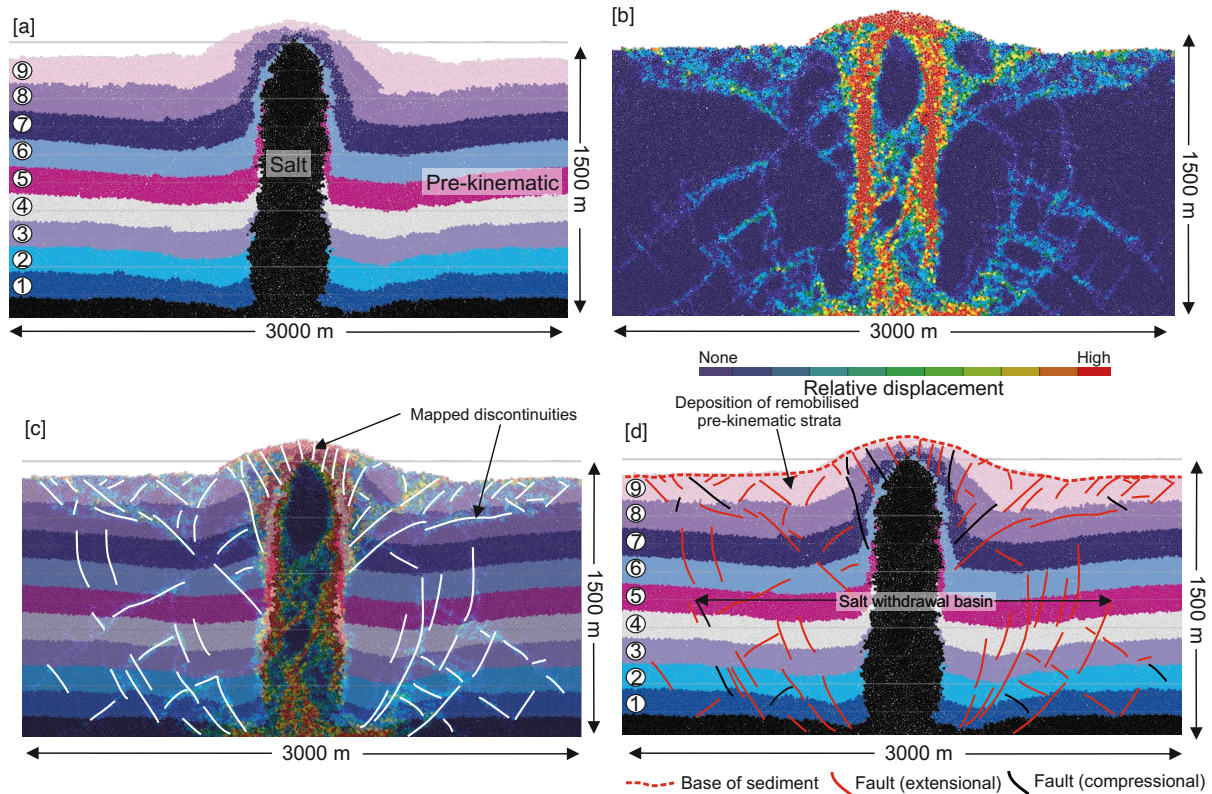


Figure 4: M1, the model with no sedimentary fill, after 4.6 Myr. Displayed outputs represent the central 3000 m of the original output model (located in Figure 3). A) Model output, uninterpreted, pre-kinematic layers are numbered for clarity, and ease of subsequent discussion. B) Static image of element displacement relative to initial neighbours for M1 after 4.6 Myr (provided for M1-M6 in Supplementary Figure 2). Cold colours represent elements that are in contact with their original neighbour and hot colours indicate high displacement. This is used to show discontinuities and is a proxy for fault location. C) (A) overlain with (B), interpreted with locations of discontinuities, highlighting the methodology used to interpret structures for all models. Note how the majority of the internal salt has remained in connection with its original neighbouring element and the radial faults are associated with salt withdrawal. The maximum displacement shows the relative movement of the salt, the neighbouring overburden, and the high mobility of layers in close proximity to the diapir. Note the lack of deformation outside of the salt withdrawal basin. D) Interpreted static DEM for 4.6 Myr, faults are taken from discontinuities in (C), and overlain onto (A).

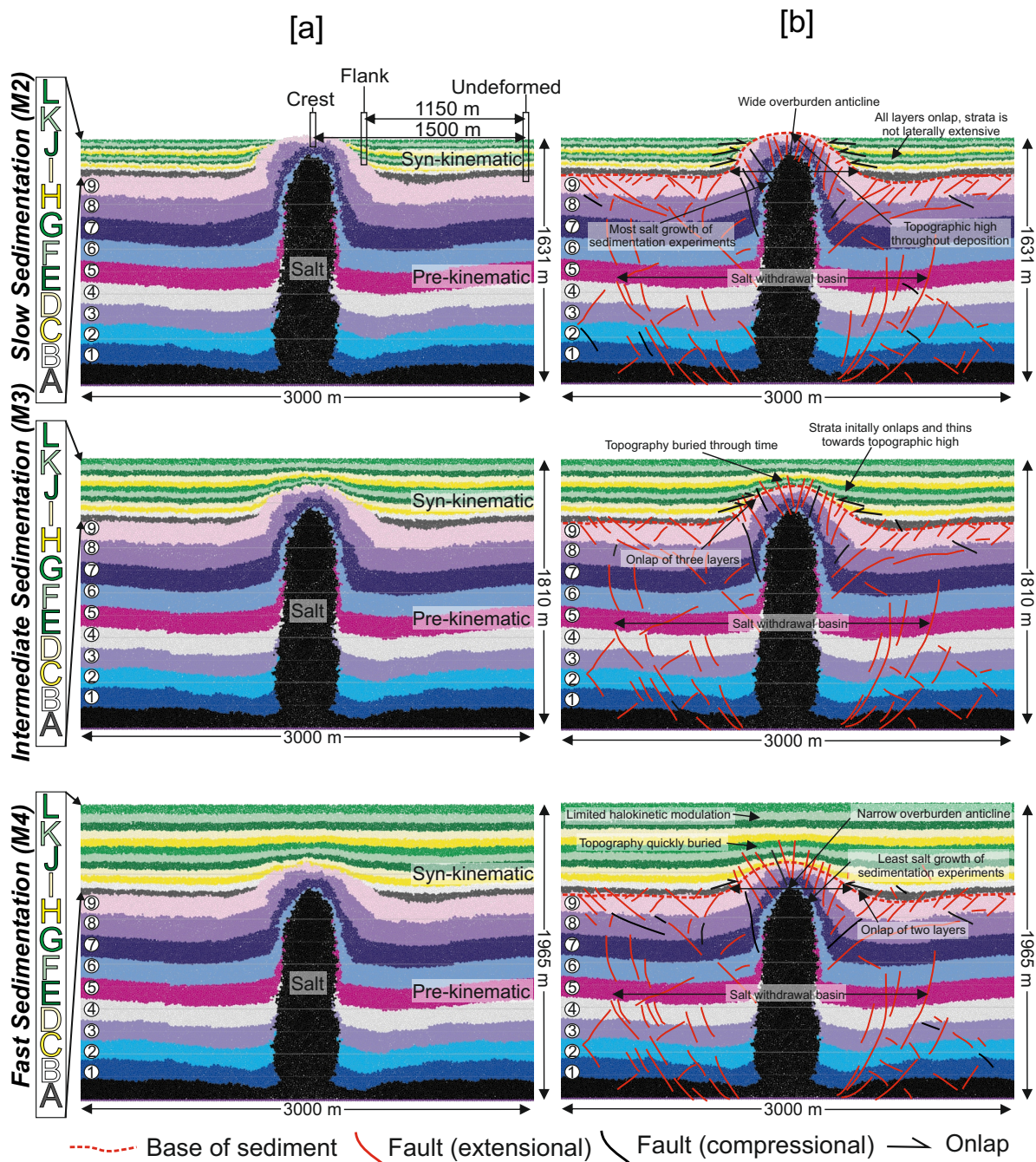


Figure 5: Uninterpreted and interpreted static images of the DEM for M2-M4 (constant sedimentation rate models) after 4.6 Myr. A) Uninterpreted models, sedimentary layers are coloured and assigned letters for easier discussion. Crest, flank and undeformed labels for M2 reflect the locations of thickness measurements taken to calculate thinning rates, this location is consistent across all models (M2-M6), B) Interpreted versions of each model. Fault interpretations use displacement from initial neighbour methodology (see Figure 4, Supplementary Figure 2). Interpretations highlight the width of salt withdrawal basins (deformed zones), height of diapirs, fault and fracture distributions, stratigraphic thickness variation and variable halokinetic influence vertically and laterally, discussed in text.

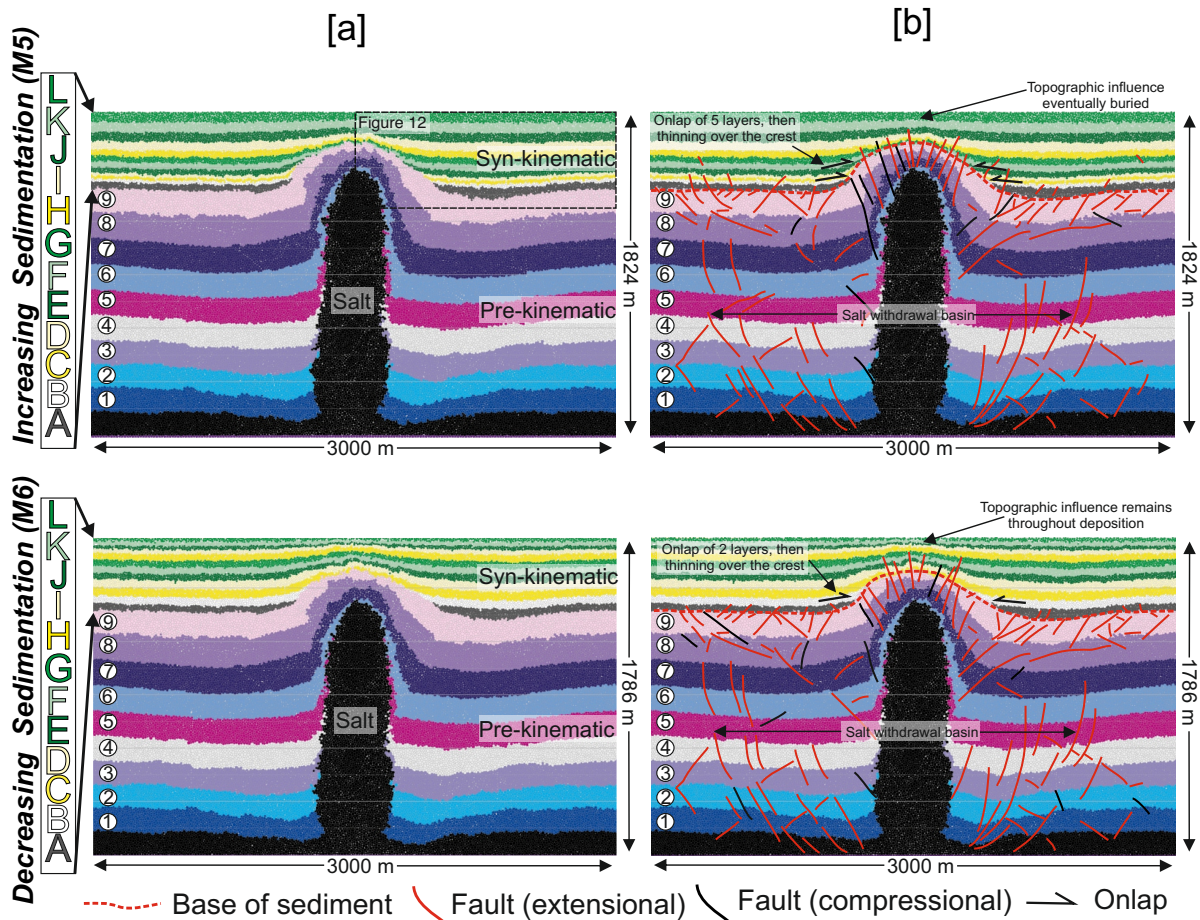


Figure 6: Uninterpreted and interpreted static image of the DEM with variable sedimentation (M5 and M6) after 4.6 Myr. Displayed output represent the central 3000 m of the original output model (located in Figure 3). A) Uninterpreted models, sedimentary layers are coloured and assigned letters for easier discussion. Crest, flank and undeformed zones mentioned in text reflect those shown in M2 (Figure 5). B) Interpreted versions of each model. Fault interpretations use displacement from initial neighbour methodology (see Figure 4, Supplementary Figure 2). Interpretations highlight the width of salt withdrawal basins (deformed zones), height of diapirs, fault and fracture distributions, stratigraphic thickness variation and variable halokinetic influence vertically and laterally discussed in text.

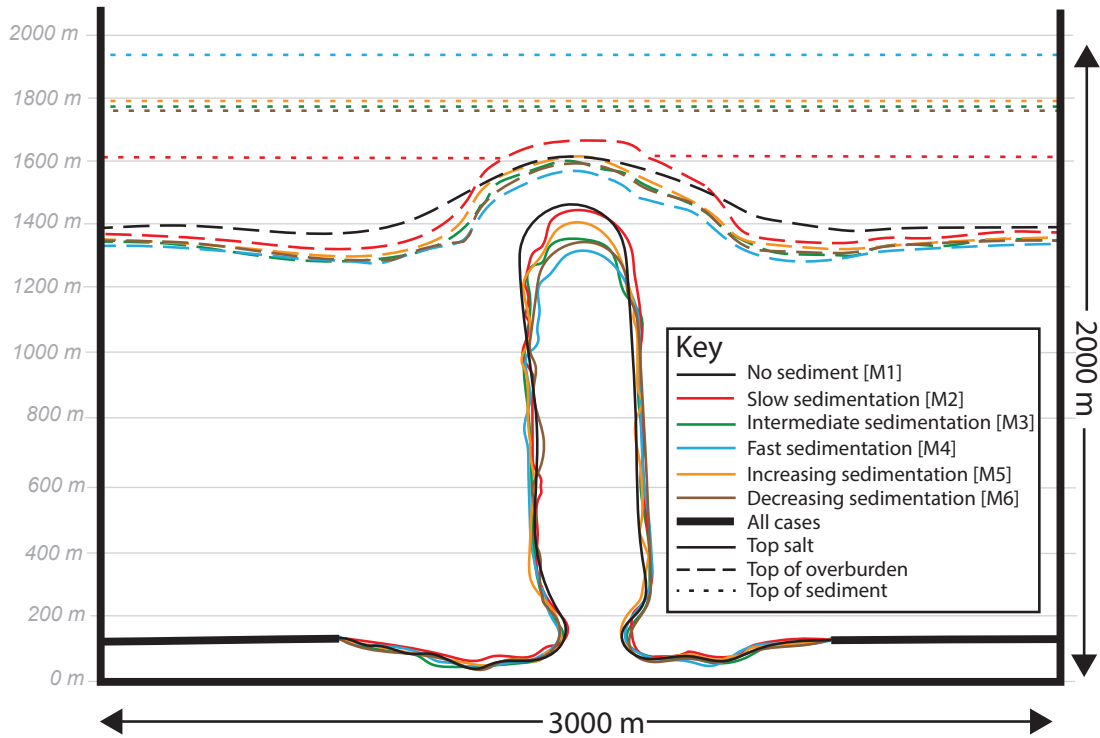


Figure 7: Diagrammatic comparison of static 4.6 Myr DEM across all models. Comparison between top salt (solid line), top of the overburden (dashed line) and top of the sediment (dotted line). The top of sediment is not shown in M1 as none is added. All cases have a similar top salt outside the deformed zone (shown by a bold black line). Diapir growth and width of the pre-kinematic overburden anticline are reduced in M2-M6 when compared to M1 due to overpressure caused by sedimentation (see Table 2). Grey lines indicate 200 metre divisions vertically. Located on Figure 3.

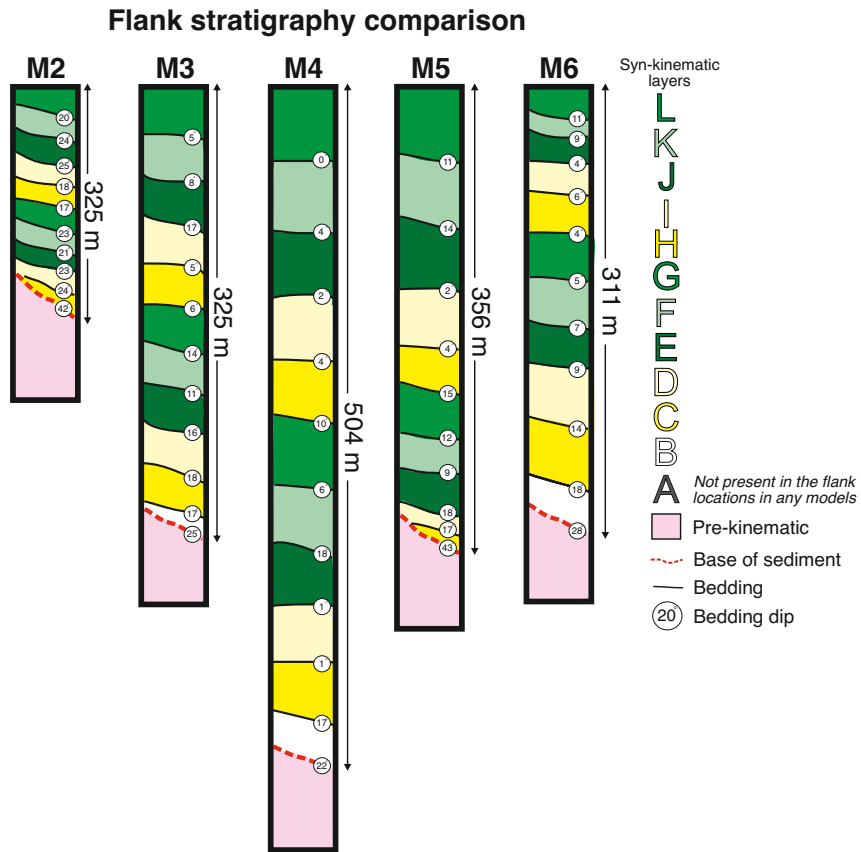
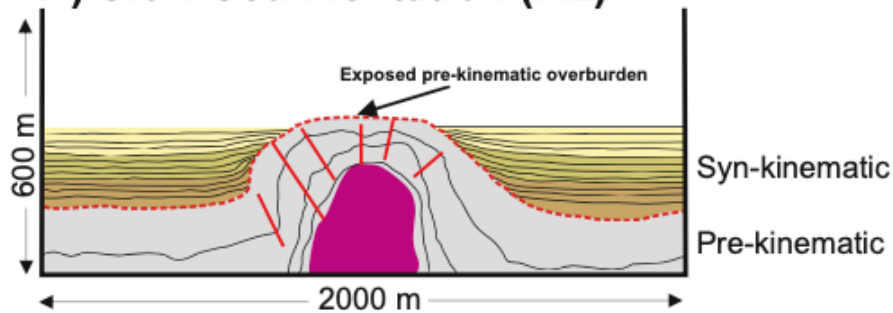


Figure 8: Comparison of stratigraphic thickness for flank location across all models with sediment (M2-M6) see Figure 5 for location of flank profile. Thicknesses and bedding orientation highlighted. The flank location shows the most deformation in all

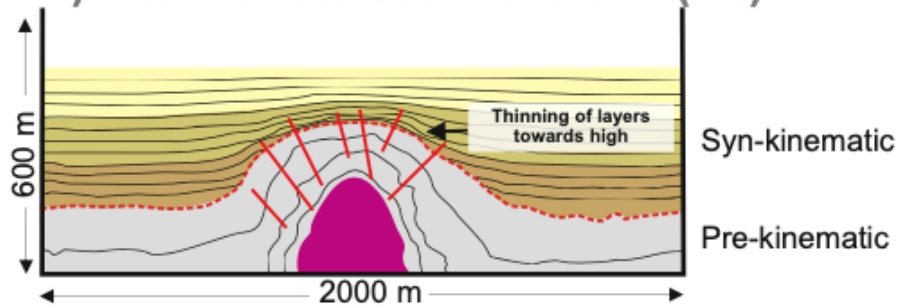
models, greatest modulation is observed in M2, and least modulation is observed in M4, generally modulation decreases upwards, however in M6 bed dip increases in layers K and L. Models give an indication of the sedimentary thickness and bed rotation expected adjacent to salt diapirs under different sedimentation rates, aiding prediction of sediment thickness and bed rotation in the subsurface salt sediment interface.

A) Slow Sedimentation (M2)



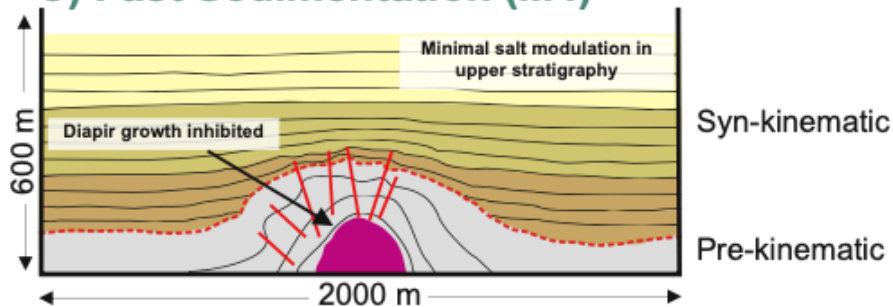
- Non-extensive layers
- Diapir forms topographic high
- Thinning towards the diapir
- Onlap onto the overburden
- Wide overburden anticline
- Long-lived salt influence

B) Intermediate Sedimentation (M3)



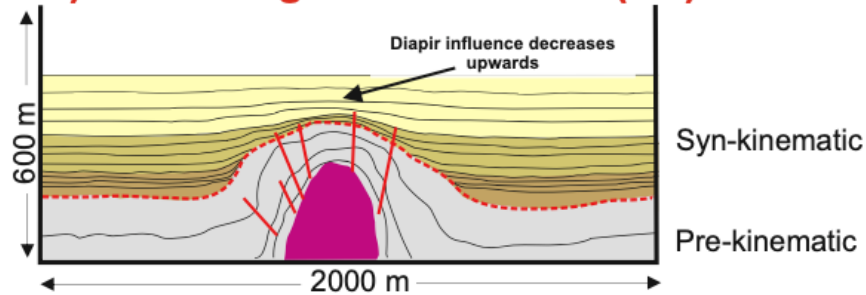
- Initially non-extensive layers
- Early overburden onlap
- Layers thin towards diapir
- Percentage thinning decreases upwards
- Halokinetic influence decreases upwards

C) Fast Sedimentation (M4)



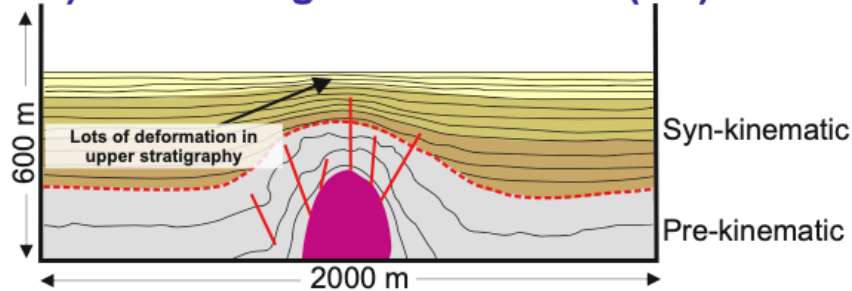
- Laterally extensive layers
- Diapir quickly buried
- Initial onlap, then thinning
- Halokinetic influence decreases upwards
- Narrow overburden anticline
- Reduced salt growth

D) Increasing Sedimentation (M5)



- Sedimentation rate rises to simulate progradation
- Initially non-extensive onlapping layers
- Then thinning of layers
- Halokinetic influence decreases upwards
- Top layer not deformed

E) Decreasing Sedimentation (M6)



- Sedimentation rate decreases to simulate retrogradation
- First layer non-extensive
- Thinning rate increases upwards
- Halokinetic influence increases upwards
- Top layers thin rapidly towards high

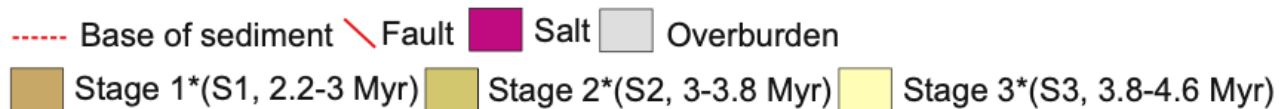


Figure 9: Schematic interpretations of M2-M6, focussed on the central 2000 m of the syn-kinematic stratigraphy, located in Figure 3. Bullet points highlight the key observations specific to each modelled scenario. Crestal faults are simplified from Figures 4 -6 to better visualise syn-kinematic stratigraphy.

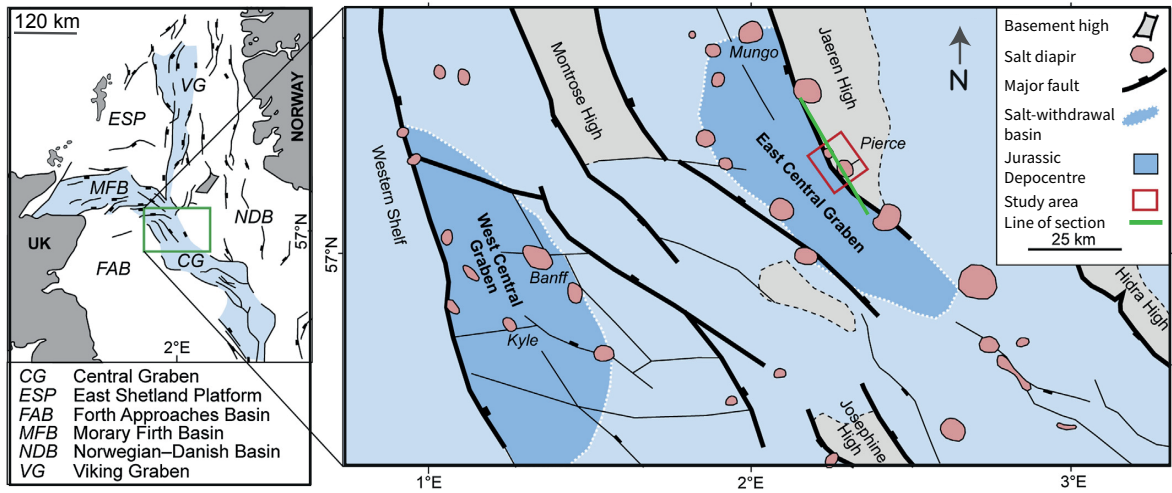


Figure 10: Tectonic framework of the North Sea rift system, and structural map of the Central Graben showing the location of salt diapirs related to major basin faults and Jurassic salt withdrawal basins (Carruthers et al. 2013). Red box locates subsurface analogue used for comparison to models and green line locates Figure 11.

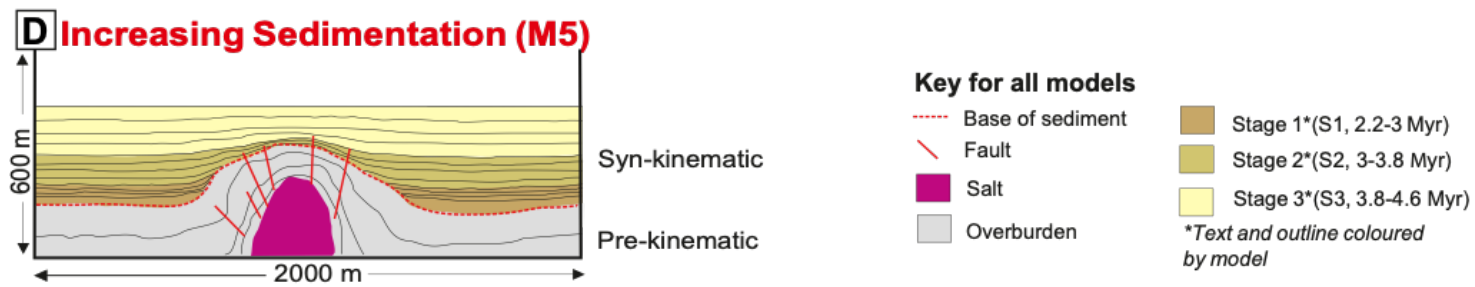
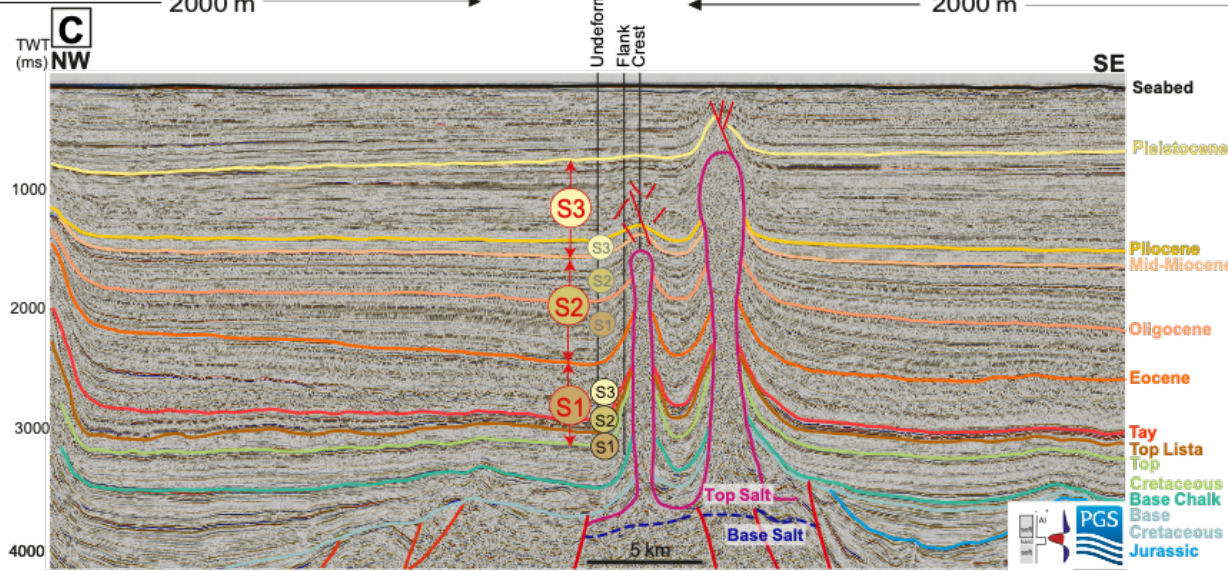
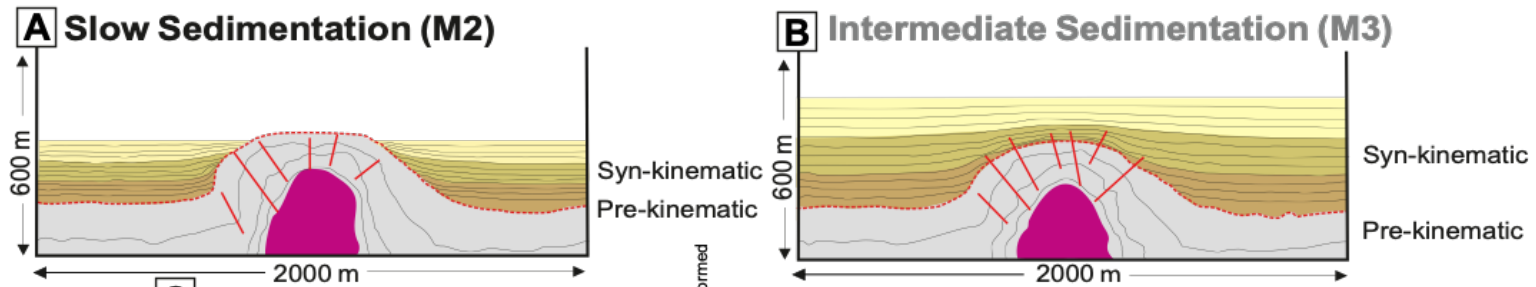


Figure 11: Subsurface example of model application comparing some of the modelled results to stratigraphy from the Pierce Field, Eastern Central Graben, UK North Sea. A,B & D) Models 2, 3 and 5 which are analogous to different parts of the stratigraphy around the Pierce diapirs. C) Interpreted time-migrated seismic profile across the Pierce diapirs. S1, S2, S3 highlight the likely sequences for comparison to models. The colour of the text represents which model those packages could represent (e.g. red represents M5). The location of the undeformed, flank and crest stratigraphic locations used for thinning rate calculations are shown for north Pierce, and are the same spacing as those used for model calculations (Figure 5; Table 3). Seismic data courtesy of PGS (MegaSurvey Plus 3D seismic data) from Cumberpatch et al. 2021b.

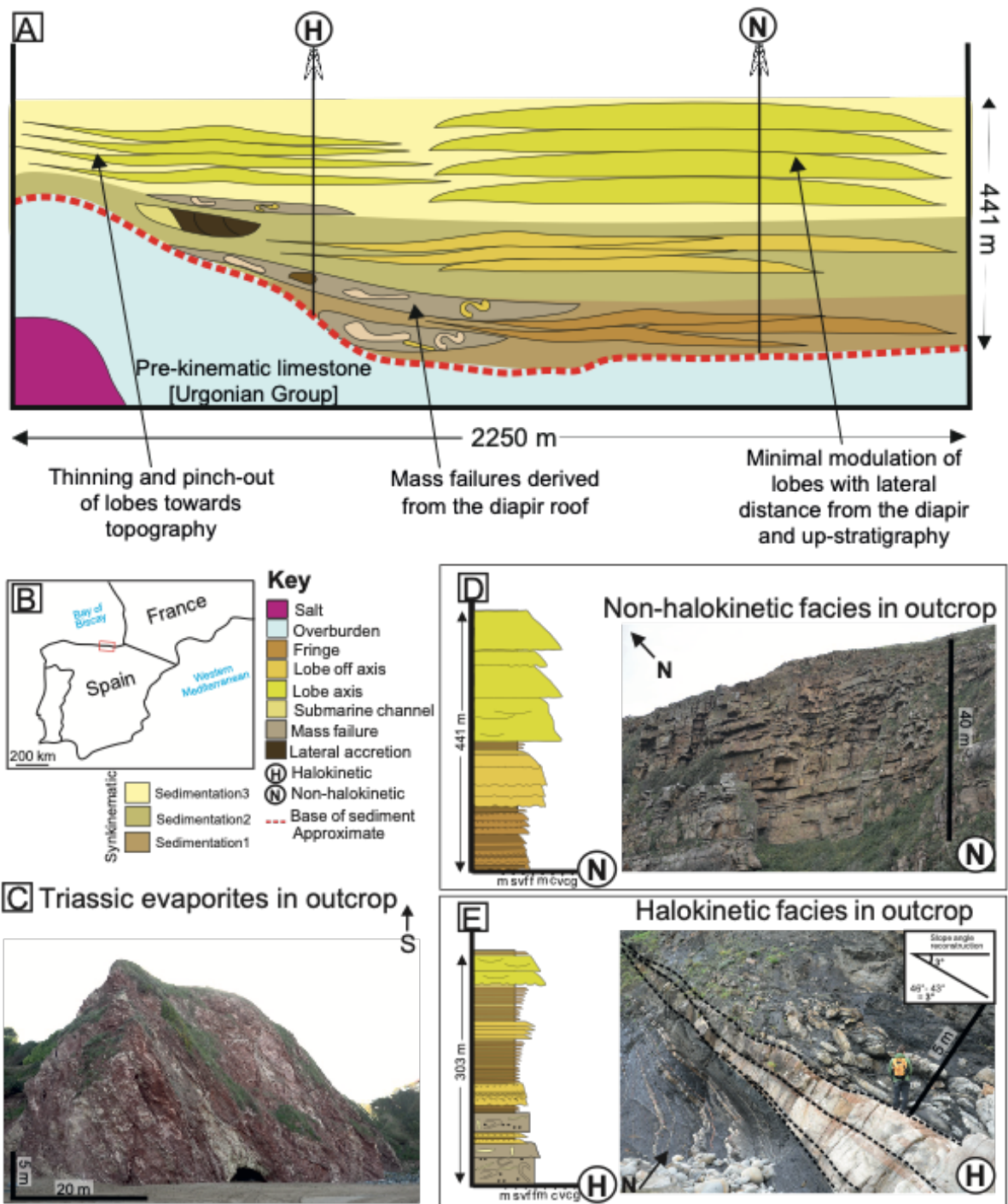


Figure 12: Conceptual facies diagram for a deep-water succession based on integration of field-based facies analysis around the Bakio diapir, Basque Cantabrian Basin Northern Spain (see Cumberpatch et al. 2021a for summary), and the result of M5. A) Deep-water facies interpretation (based on field facies analysis) for the upper part of the increasing sedimentation model (located on Figure 6). H and A are theoretical stratigraphic profiles in the halokinetically-influenced and non-halokinetically-influenced zones respectively. B) Location map of the field analogue, for a full geological discussion see Cumberpatch et al. in 2021a). C) Outcropping Triassic evaporites on Bakio Beach, believed to be part of the Bakio Diapir. D) Non-halokinetic succession showing a classic progradational deep-water system (controlled by allogenic and autogenic processes), accompanied by an example of non-halokinetically influenced strata from the field. E) Halokinetic stratigraphic profile showing a thinner, modulated succession which is rich in MTDs, accompanied by a field analogue of an outcrop-scale bed pinch-out and an overlying MTD.

Example of Halokinetic Zonation (M3)

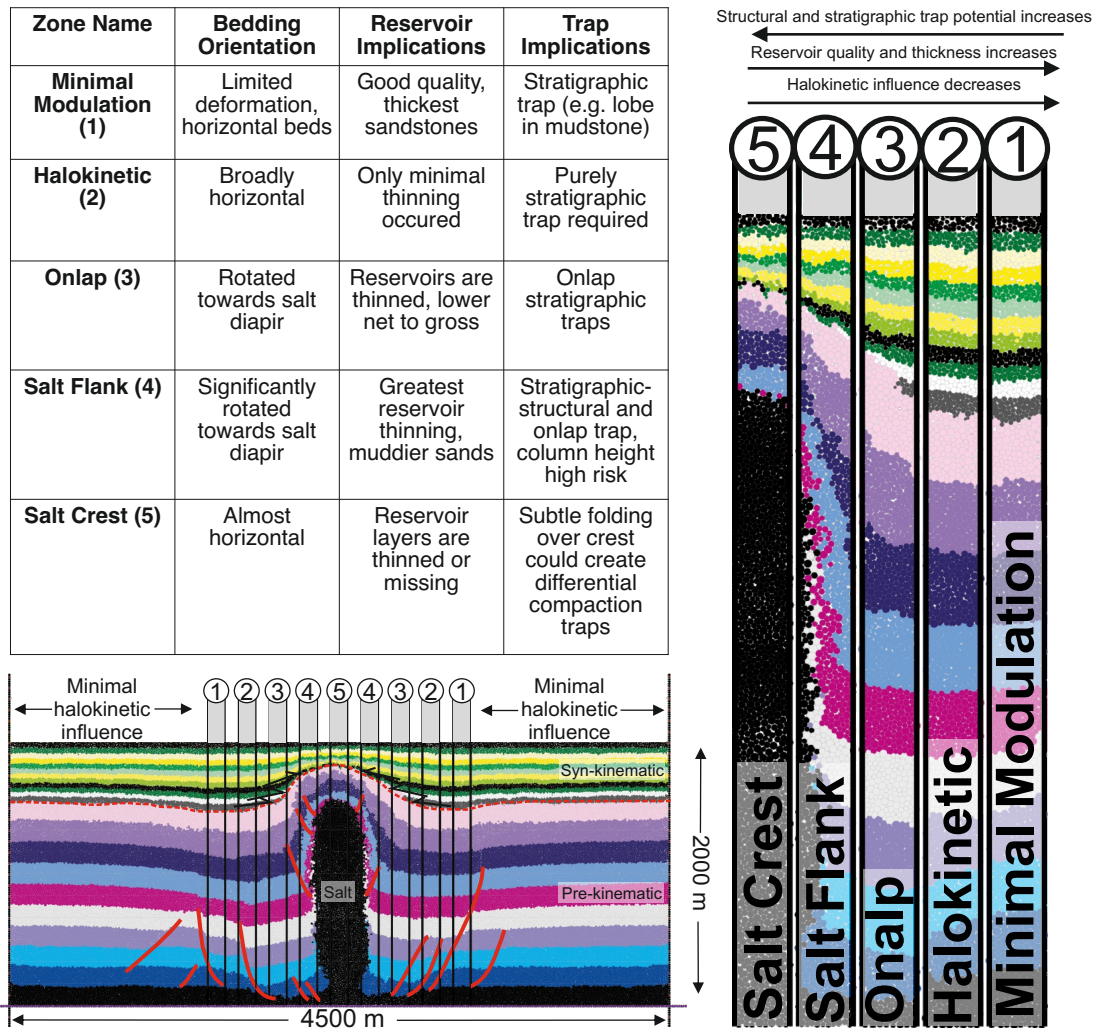


Figure 13: Halokinetic zonation scheme shown for M3. The model is divided into 5 zones, 4 of which experience some form of halokinetic influence. Minimal deformation zones 1 and all stratigraphy outside of it show virtually no modulation by salt diapirism. Halokinetic influence increases towards the diapir-cored high, and changes from thinning in the ‘halokinetic’ zone to onlap and abrupt pinch out in the ‘onlap’ and ‘salt flank’ zones. Thinned and reduced stratigraphy are observed over the diapirs crest. The table highlights that while stratigraphic trap quality may be greater closer to the diapir, reservoir thickness and quality are likely higher further from the diapir, showing a ‘trade-off’ exists for subsurface energy exploration and production. Similar zonation is possible for all models.

Model	Sedimentation Type	Sedimentation Interval		
		S1 (2.2-3.0 Myr) [22000 – 30000 time steps]	S2 (3.0-3.8 Myr) [30000 – 38000 time steps]	S3 (3.8-4.6 Myr) [3800 – 46000 time steps]
		Sedimentation Rate (mm/year)		
M1	None	0.0	0.0	0.0
M2	Slow consistent sedimentation (Aggradation)	0.15	0.15	0.15
M3	Intermediate consistent sedimentation (Aggradation)	0.30	0.30	0.30
M4	Fast consistent sedimentation (Aggradation)	0.45	0.45	0.45
M5	Increasing sedimentation (Progradational)	0.15	0.30	0.45
M6	Decreasing sedimentation (Retrogradational)	0.45	0.30	0.15

Table 1: Details of the different sedimentation patterns and rates used in the six experiments. S1-3 refer to sedimentation intervals.

Model	Diapir growth (upward movement) (m)	Percentage reduction compared to base case (M1)	Pre-kinematic folded roof width (m)	Percentage reduction compared to base case (M1)	Syn-kinematic folded roof width (m)	Ratio of syn- : pre-kinematic folded roof (m)
M1, No sedimentation	425	n/a	961	n/a	n/a	n/a
M2, Slow sedimentation rate	393	8	770	20	n/a	n/a
M3, Intermediate sedimentation rate	363	15	760	21	839	1.1
M4, Fast sedimentation rate	297	30	734	24	890	1.21
M5, Increasing sedimentation rate	368	14	750	22	723	0.96
M6, Decreasing sedimentation rate	346	19	753	22	872	1.16

Table 2: Comparison of diapir growth and overburden anticline width across all six experiments at T=4.6 Myr. Measurements are taken from model simulations (Figure 4, 5 and 6). Initial diapir height (1050 m at T=0 Myr) is subtracted from final diapir height to give diapir growth. M2-6 are compared to M1 to show the percentage reduction that occurs when different amounts of sediment are added. Pre-kinematic anticline measurements are taken from the stratal termination of layer A, in M1 they are taken from the top of the overburden at the location of the greatest change in dip. For M2-M6 the width of the overburden is compared to M1 to show the percentage reduction in overburden anticline width that occurs when different amounts of sediment are added. Syn-kinematic folded roof measurement are taken from location of greatest dip change in layer F (Supplementary Figure 1). Value only calculated where layers extend across the entire structure (M3-M6). Ratio of syn- to pre-kinematic folded roof thickness is calculated.

Model	U-C (%)	U-C (%/m)	U-F (%)	U-F (%/m)	F-C (%)	F-C (%/m)	U-F:F-C
Slow (M2)	-	-	34.4	0.029	-	-	-
Intermediate (M3)	54.5	0.037	19.2	0.017	35.3	0.1	1:6.1
Layers B & C [~S1]	-	-	26.4	0.023	-	-	-
Layers D-H [~S2]	60.1	0.040	14.5	0.011	45.6	0.13	1:10.3
Layers I-L [S3]	23.2	0.015	6.3	0.005	16.9	0.048	1:8.8
Fast (M4)	32.5	0.022	11.6	0.010	20.9	0.060	1:5.9
Layer B [Early S1]	-	-	47.0	0.041	-	-	-
Layers C & D [Late S1]	38.4	0.026	12.9	0.011	25.5	0.073	1:6.5
Layers E-H [S2]	29.7	0.019	8.6	0.007	21.1	0.06	1:8
Layers I-L [S3]	2.35	0.0016	1.04	0.0009	1.3	0.037	1:4.1
Increasing (M5)	58.3	0.039	19.3	0.017	38.9	0.11	1:6.6
Layers B-D [S1]	-	-	61.1	0.053	-	-	-
Layer E [Early S2]	-	-	24.8	0.0022	-	-	-
Layers F-H [Late S2]	60.6	0.040	15.9	0.014	44.8	0.128	1:9.2
Layers I-L [S3]	21.5	0.014	6.7	0.006	14.7	0.042	1:7.2
Decreasing (M6)	52.4	0.035	18.6	0.016	33.9	0.097	1:5.9
Layer B [Early S1]	-	-	37.4	0.017	-	-	-
Layers C&D [Late S1]	39.6	0.026	10.3	0.009	29.3	0.084	1:9.3
Layers E-H [S2]	42.3	0.028	11.4	0.009	30.8	0.088	1:8.8
Layers I-L [S3]	43.9	0.029	19.5	0.017	24.5	0.069	1:4.1

Table 3: Comparison of stratigraphic thinning across M2-M6. Bold headings indicate each model and show the total thinning for all stratigraphy, beneath each heading this is divided by sedimentary package. Layer A is excluded as it fills to base level in all models. Layers are subdivided based on observational differences (e.g. lateral extent across the model) and are broadly grouped into their sedimentation stage (S1, S2, S3). Percentage thinning and normalised thinning rates (%/m) are shown for U-C (Undeformed to Crest, i.e., the total model), U-F (Undeformed to Salt Flank) and F-C (Salt Flank to Crest). In layers which do not extend across the entire model no results exist for U-C and F-C. The final column displays the ratio of the normalised thinning rate between the Undeformed to Salt Flank and the Salt Flank to Crest sections, to show how much more thinning is observed adjacent to the diapir. Locations of undeformed, flank and crest measurements are shown on Figure 5, and are the same for all models to ensure direct comparison.